Spring 2018

# Facile synthesis of nanostructured metal borides and composites for applications in sustainable energy

Maalavan Arivu



Department:

# FACILE SYNTHESIS OF NANOSTRUCTURED METAL BORIDES AND COMPOSITES FOR APPLICATIONS IN SUSTAINABLE ENERGY

by

MAALAVAN ARIVU

A THESIS

Presented to the Faculty of the Graduate School of the

MISSOURI UNIVERSITY OF SCIENCE AND TECHNOLOGY

In Partial Fulfillment of the Requirements for the Degree

MASTER OF SCIENCE IN MATERIALS SCIENCE AND ENGINEERING

2018

Approved by

Dr. Manashi Nath, Advisor
Dr. William G. Fahrenholtz
Dr. Fatih Dogan

## PUBLICATION THESIS OPTION

This thesis has been prepared in the form of journal article formatted to the specifications prescribed by Missouri University of Science and Technology.

The paper, pages 33 to 47 has been published in Electrochemistry Communications, a journal of Elsevier.

## ABSTRACT

Electrocatalytic water splitting is a promising solution for sustainable energy generation since one of the half reactions lead to the formation of $H_2$ which is a clean fuel. The other half of the reaction leading to $O_2$ evolution is an energy intensive process necessitating the need for an electrocatalyst to break the activation barrier for the commencement of the reaction. In this work we will focus on expanding the family of non-oxidic OER electro-catalysts, especially borides, whereby, apart from facilitating delocalization of electron cloud on the catalytically active transition metal site, low anion electronegativity and increased covalency in the lattice compared to oxides, is expected to facilitate the catalytic process. Analyzing these properties, amorphous nickel boride ($Ni_3B$) was chosen and synthesized through a room temperature chemical conversion technique. Characterization of the synthesized material confirmed that the as-prepared $Ni_3B$ was nanocrystalline with particles in the range of 50 – 60nm. $Ni_3B$ showed high efficiency for electrocatalytic $O_2$ evolution under alkaline conditions exhibiting a low onset potential and overpotential ($\eta$) of 340 mV @ 10 $mAcm^{-2}$. $Ni_3B$ was further incorporated into a matrix of reduced graphene oxide to improve the catalytic performance by facilitating charge transfer within the catalytic matrix since its incorporation increases conductivity of the catalytic film. As expected, $Ni_3B$-reduced graphene oxide nanocomposite showed an improved catalytic performance compared to $Ni_3B$ nanostructures with onset potential lower by 70mV and $\eta$ of 290 mV @ $10mAcm^{-2}$. The OER catalytic performance obtained with $Ni_3B$ and nanocomposite was observed to be significantly better than the conventionally used noble metal oxides such as $RuO_x$, and was comparable to some of the best OER electrocatalysts.

# ACKNOWLEDGMENTS

Firstly, I would like to express my sincere gratitude to my advisor, Dr. Manashi Nath, for her patience, guidance, encouragement, and support throughout the study of my masters'. Her dispassionate commitment to research and hard work are the two motivating factors that kept me going through out my masters' and gain immense knowledge both practically and theoretically. I would also like to thank my committee members Dr. William G.Fahrenholtz and Dr. Fatih Dogan for their guidance and support.

Secondly, I would like to thank American Chemical Society (ACS) for providing the Petroleum Research Fund [54793-ND10] and CASB, Missouri University of Science and Technology for their financial support. I would also like to thank the Materials Research Center of Missouri University of Science and Technology for the usage of their equipment.

Last but not least, I would like to thank my parents for believing in me and supporting me in all my deeds. I would also like to thank my lab mates and friends who have always been supportive.

# TABLE OF CONTENTS

SECTION

# LIST OF ILLUSTRATIONS

PAPER



SECTION

# LIST OF TABLES

# 1. INTRODUCTION

Man's profound exploitation of non-renewable resources for energy generation has had a negative impact on the environment. The technologies that have been developed in the past are mostly fueled by fossil fuels [1]. Extensive usage of these resources has not only resulted in their depletion, but also has resulted in large scale pollution. For example, combustion of carbon based energy sources lead to the formation of greenhouse gases such as $CO_2$, CO, etc. [2], which ultimately lead to global warming. This necessitates the need to develop renewable resources for clean energy generation that on usage does not lead to environmental pollution. There is a need for developing means to generate sustainable energy. Sustainable energy is one which is consumed at negligible rate compared to its supply [3]. Solar energy, wind energy and energy derived from water are some of the most promising sources of sustainable energy [4]. Among these electrocatalytic water splitting shows tremendous promise for generation of clean energy with zero pollution, and is one of the primary reactions for a variety of energy conversion devices such as fuel cells, metal-air batteries, and solar-to-fuel energy conversion devices. While solar energy harnesses the power of the sun and converts that to electricity, water electrolysis stores energy in chemical bonds that can be delivered and used as desired. Hence, this technology complements solar energy conversion by providing a source of useable energy in absence of direct sunlight, and is becoming increasingly important in grid-based energy generation technology.

## 1.1. ELECTROLYSIS OF WATER

Electrocatalytic water splitting involves two half-cell reactions: hydrogen evolution reaction (HER) occurring at the cathode and oxygen evolution reaction (OER) at the anode as shown in Figure 1.1. Hydrogen is a clean fuel which on combustion does not lead to the generation of any greenhouse gases [5]. The electrocatalytic water splitting is a clean way of producing hydrogen when compared to that of conventional means of production by combustion of natural gas, coal, etc. [5]. Oxygen evolution reaction, on the other hand, is a sluggish process requiring high energy to break the activation barrier. Typically electrocatalysts are used to reduce the activation barrier reflected in the lowering of applied potential to initiate the catalytic reaction. The oxygen evolution reaction in alkaline medium starts with the attachment of the $OH^-$ ions on the catalytically active surface site. Hence, the coordination and ligand environment around the catalytically active metal site plays a crucial role in determining the chemical potential and OER catalytic activity. Although traditionally, precious metals and precious metal oxides such as those of Ru, Ir and Pt were the most commonly used OER electrocatalysts, recently transition metal based compounds have shown very promising catalytic activity outperforming the precious metal oxides. A thorough literature review regarding the various classes of OER electrocatalysts has been provided in Section 1.4 and 1.5, where it has also been explained how OER activity can be made more efficient by altering the local coordination environment around the transition metal site through hypothesis driven materials chemistry. In the case of metal borides, the degree of covalency in the metal-boron interaction as well as the Lewis acidity of the surface sites facilitates efficient attachment of $OH^-$ ions and hence promotes initiation of OER. This favorable property

has been exploited for application of metal borides as electrocatalysts for OER in this work. The catalytic performance can further be improved by introducing carbon based materials into the system which facilitate better electron transfer between catalyst surface and substrate. Carbon based materials such as reduced graphene oxide, graphene oxide, carbon nanotubes, etc. are combined with electrocatalysts to improve catalytic performance through synergistic effect. Sections 1.3-1.11 provide detailed explanation of mechanism of catalytic OER process, different families of electrocatalysts, as well as the electrochemical studies for determining OER catalytic activity.

**Anode:** $4OH^- \rightarrow O_2 + 2H_2O + 4e^-$

**Cathode:** $4H_2O + 4e^- \rightarrow 2H_2 + 4OH^-$

**Overall:** $2H_2O \rightarrow O_2 + 2H_2$

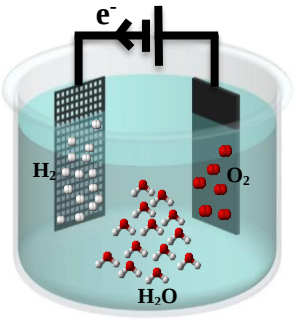


Figure 1.1. Overall water splitting reaction consisting of two half reactions of oxygen evolution and hydrogen evolution.

Typically water electrolysis process is carried out from room temperature to 200$^o$C (low temperature electrolysis) or 500$^o$C to 1000$^o$C (high temperature electrolysis). Interestingly in the intermediate range, water electrolysis technologies has not been extensively developed.

Based on the charge carrier, water electrolysis can be further divided into three types. Alkaline ($OH^-$) electrolysis, proton exchange ($H^+$) electrolysis and oxygen ion ($O^{2-}$) electrolysis with charge carriers as $OH^-$, $H^+$ and $O^{2-}$ respectively as shown in Figure 1.2 [6] below. Water electrolysis is the core process in a fuel cell. Alkaline water electrolysis

is the most mature technology of all, which is being employed extensively in commercial scale. This work is focused on alkaline water electrolysis and addressing the challenges in it.

| | Low Temperature Electrolysis | | | High Temperature Electrolysis | | |
|---|---|---|---|---|---|---|
| | Alkaline ($OH^-$) electrolysis | | Proton Exchange ($H^+$) electrolysis | Oxygen ion($O^{2-}$) electrolysis | | |
| | Liquid | Polymer Electrolyte Membrane | | Solid Oxide Electrolysis (SOE) | | |
| | Conventional | Solid alkaline | $H^+$ - PEM | $H^+$ - SOE | $O^{2-}$ - SOE | Co-electrolysis |
| Operation principles | 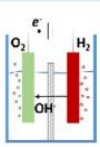 | 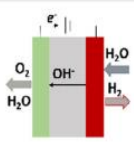 | 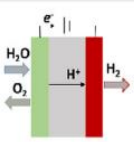 | 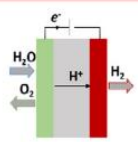 | 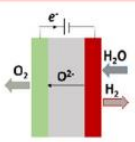 | 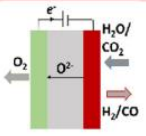 |
| Charge carrier | $OH^-$ | $OH^-$ | $H^+$ | $H^+$ | $O^{2-}$ | $O^{2-}$ |
| Temperature | 20-80°C | 20-200°C | 20-200°C | 500-1000°C | 500-1000°C | 750-900°C |
| Electrolyte | liquid | solid (polymeric) | solid (polymeric) | solid (ceramic) | solid (ceramic) | solid (ceramic) |
| Anodic Reaction (OER) | $4OH^- \rightarrow 2H_2O + O_2 + 4e^-$ | $4OH^- \rightarrow 2H_2O + O_2 + 4e^-$ | $2H_2O \rightarrow 4H^+ + O_2 + 4e^-$ | $2H_2O \rightarrow 4H^+ + 4e^- + O_2$ | $O^{2-} \rightarrow {}^1/_2O_2 + 2e^-$ | $O^{2-} \rightarrow {}^1/_2O_2 + 2e^-$ |
| Anodes | Ni > Co > Fe (oxides) Perovskites: $Ba_{0.5}Sr_{0.5}Co_{0.8}Fe_{0.2}O_{3-\delta}$, $LaCoO_3$ | Ni-based | $IrO_2$, $RuO_2$, $Ir_xRu_{1-x}O_2$ Supports: $TiO_2$, ITO, TiC | Perovskites with protonic-electronic conductivity | $La_xSr_{1-x}MnO_3$ + Y-Stabilized $ZrO_2$ (LSM-YSZ) | $La_xSr_{1-x}MnO_3$ + Y-Stabilized $ZrO_2$ (LSM-YSZ) |
| Cathodic Reaction (HER) | $2H_2O + 4e^- \rightarrow 4OH^- + 2H_2$ | $2H_2O + 4e^- \rightarrow 4OH^- + 2H_2$ | $4H^+ + 4e^- \rightarrow 2H_2$ | $4H^+ + 4e^- \rightarrow 2H_2$ | $H_2O + 2e^- \rightarrow H_2 + O^{2-}$ | $H_2O + 2e^- \rightarrow H_2 + O^{2-}$ $CO_2 + 2e^- \rightarrow CO + O^{2-}$ |
| Cathodes | Ni alloys | Ni, Ni-Fe, $NiFe_2O_4$ | Pt/C $MoS_2$ | Ni-cermets | Ni-YSZ Subst. $LaCrO_3$ | Ni-YSZ perovskites |
| Efficiency | 59-70% | | 65-82% | up to 100% | up to 100% | - |
| Applicability | commercial | laboratory scale | near-term commercialization | laboratory scale | demonstration | laboratory scale |
| Advantages | low capital cost, relatively stable, mature technology | combination of alkaline and $H^+$-PEM electrolysis | compact design, fast response/start-up, high-purity $H_2$ | enhanced kinetics, thermodynamics: lower energy demands, low capital cost | | + direct production of syngas |
| Disadvantages | corrosive electrolyte, gas permeation, slow dynamics | low $OH^-$ conductivity in polymeric membranes | high cost polymeric membranes; acidic: noble metals | mechanically unstable electrodes (cracking), safety issues: improper sealing | | |
| Challenges | Improve durability/reliability; and Oxygen Evolution | Improve electrolyte | Reduce noble-metal utilization | microstructural changes in the electrodes: delamination, blocking of TPBs, passivation | | C deposition, microstructural change electrodes |

Figure 1.2. Classification of electrolysis based on temperature, charge carrier and electrolyte.[6]

## 1.2. WATER ELECTROLYSIS IN ALKALINE CONDITIONS: CHALLENGES AND SOLUTION

When a potential gradient is applied, there is movement of electrons leading to the production of current. The thermodynamics of half reaction shown in Table 1.1 is defined on an absolute potential ($E^\circ$) scale, $\Delta G^\circ = nFE^\circ$ as shown in the table below. Where n =

number of electrons transferred in the overall reaction, F = Faraday's constant [7]. The potential scale can be shifted based on the reference electrode used [7]. Electrochemical measurements on the working electrode in an electrochemical cell are made with respect to the reference electrode. Reduction of $2H^+$ to $H_2$ (g) is assumed to be occurring at an absolute potential of 0.00V and the electrode at which this reaction takes place is called 'Reversible Hydrogen Electrode' (RHE) [8].

The thermodynamic water splitting potential is 1.23V. This is the ideal and theoretical value of the energy required for OER to take place. However, the reaction in reality requires a higher energy than required to break the activation barrier. A catalytic material that can break the activation barrier and lead to the commencement of OER is required.

The potential at which OER starts is called the onset potential. OER is also a kinetically sluggish reaction [6]. It is a four electron ($4e^-$) process involving the double bond formation between two oxygen atoms to form $O_2$ [6]. So, energy that is supplied in excess of 1.23V is called overpotential denoted by 'η'. $\eta = E_{appl} - 1.23V$, where $E_{appl}$ = applied potential.

Extensive amount of research is going on in bringing down the onset potential and the overpotential as close as possible to 1.23V. It is important to bring down the onset potential and overpotential for OER in water splitting and this is the challenge faced in alkaline water electrolysis [6].

The materials that enable this are called 'electrocatalysts'. Electrocatalytic materials bring down the activation energy required for the reaction to start as shown in the Figure 1.3 below.

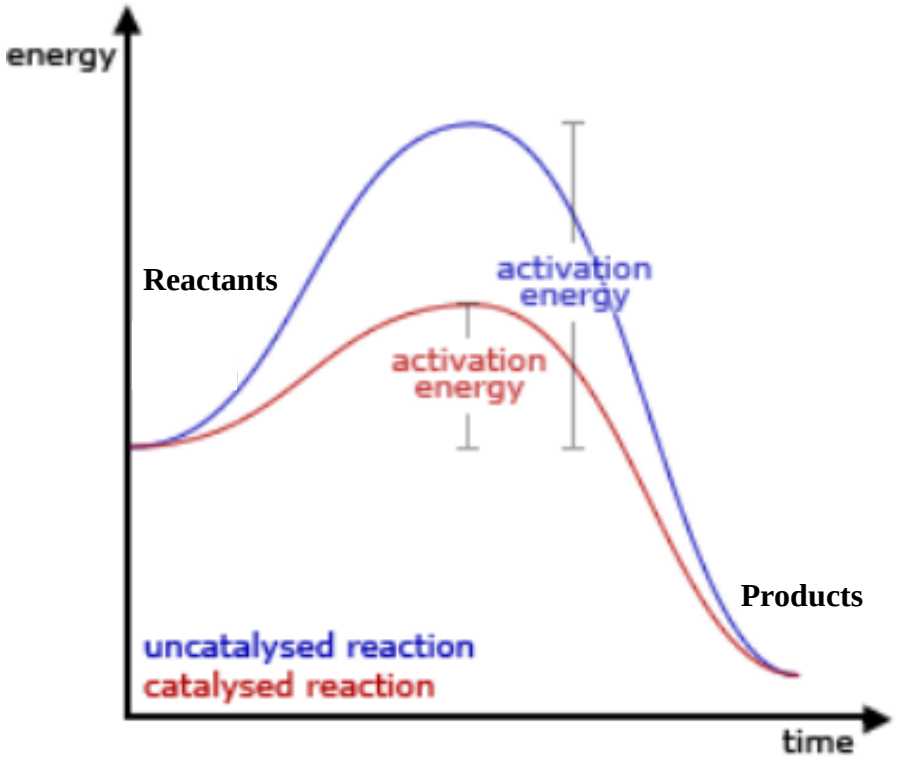


Figure 1.3. Activation energy variation in an energy vs time plot between uncatalyzed and catalyzed reaction. [7]

Typically, the current produced by the application of potential is normalized with geometric electrode area and reported as current density [9,10].

Apart from electrocatalysts, scientists are also developing photocatalysts and photoelectrochemical catalysts which can utilize solar energy for water splitting reaction. These systems mimic photosynthesis and this direction of research is generically referred to as artificial photosynthesis [9].

To benchmark the different catalysts being reported researchers have identified $\eta$ at 10 $mAcm^{-2}$ current density as a standard to estimate the catalyst performance [9,10]. Hence in our research we have compared $\eta$ at 10 $mAcm^{-2}$ with other reported catalysts in Section 1.5 & Section 3 of paper.

Table 1.1. List of Cathodic half reactions and their corresponding standard reduction potentials. [11]

| Cathode (Reduction) Half-Reaction | Standard Potential $E^{\circ}$ (volts) |
|---|---|
| $Zn^{2+}(aq) + 2e^- \rightarrow Zn(s)$ | -0.76 |
| $Cr^{3+}(aq) + 3e^- \rightarrow Cr(s)$ | -0.74 |
| $Fe^{2+}(aq) + 2e^- \rightarrow Fe(s)$ | -0.41 |
| $Cd^{2+}(aq) + 2e^- \rightarrow Cd(s)$ | -0.40 |
| $Ni^{2+}(aq) + 2e^- \rightarrow Ni(s)$ | -0.23 |
| $Sn^{2+}(aq) + 2e^- \rightarrow Sn(s)$ | -0.14 |
| $Pb^{2+}(aq) + 2e^- \rightarrow Pb(s)$ | -0.13 |
| $Fe^{3+}(aq) + 3e^- \rightarrow Fe(s)$ | -0.04 |
| $2H^+(aq) + 2e^- \rightarrow H_2(g)$ | 0.00 |
| $Sn^{4+}(aq) + 2e^- \rightarrow Sn^{2+}(aq)$ | 0.15 |
| $Cu^{2+}(aq) + e^- \rightarrow Cu^+(aq)$ | 0.16 |
| $ClO_4^-(aq) + H_2O(l) + 2e^- \rightarrow ClO_3^-(aq) + 2OH^-(aq)$ | 0.17 |
| $AgCl(s) + e^- \rightarrow Ag(s) + Cl^-(aq)$ | 0.22 |
| $Cu^{2+}(aq) + 2e^- \rightarrow Cu(s)$ | 0.34 |
| $ClO_3^-(aq) + H_2O(l) + 2e^- \rightarrow ClO_2^-(aq) + 2OH^-(aq)$ | 0.35 |
| $IO^-(aq) + H_2O(l) + 2e^- \rightarrow I^-(aq) + 2OH^-(aq)$ | 0.49 |
| $Cu^+(aq) + e^- \rightarrow Cu(s)$ | 0.52 |
| $ClO_2^-(aq) + H_2O(l) + 2e^- \rightarrow ClO^-(aq) + 2OH^-(aq)$ | 0.59 |
| $Fe^{3+}(aq) + e^- \rightarrow Fe^{2+}(aq)$ | 0.77 |
| $Hg_2^{2+}(aq) + 2e^- \rightarrow 2Hg(l)$ | 0.80 |
| $Hg^{2+}(aq) + 2e^- \rightarrow Hg(l)$ | 0.85 |
| $ClO^-(aq) + H_2O(l) + 2e^- \rightarrow Cl^-(aq) + 2OH^-(aq)$ | 0.90 |
| $NO_3^-(aq) + 4H^+(aq) + 3e^- \rightarrow NO(g) + 2H_2O(l)$ | 0.96 |
| $Br_2(l) + 2e^- \rightarrow 2Br^-(aq)$ | 1.07 |
| $O_2(g) + 4H^+(aq) + 4e^- \rightarrow 2H_2O(l)$ | 1.23 |
| $Cr_2O_7^{2-}(aq) + 14H^+(aq) + 6e^- \rightarrow 2Cr^{3+}(aq) + 7H_2O(l)$ | 1.33 |

## 1.3. MECHANISM OF OER AT THE CATALYTIC SITE AND THE EFFECT OF SURFACE ATOM

OER in alkaline medium is a multi-step process with each elementary step generating one electron. A typical OER reaction on the catalyst surface can be explained from the modified Krasil'shchikov mechanism originally proposed for metallic anode OER catalysis. This has been later adapted by several other researchers for metal oxidic and non-oxidic electrocatalyzed OER [12-16] and the mechanism is as follows,

$$[S]^n + OH^- \rightarrow [S^{n+1}\text{-}OH] + e^-\text{----------Eq.=1}$$

$$[S^{n+1}\text{-}OH] + OH^- \rightarrow [S^{n+1}\text{-}O]^- + H_2O\text{-------Eq.=2}$$

$$[S^{n+1}\text{-}O]^- \rightarrow [S^n\text{-}O] + e^-\text{----------Eq.=3}$$

$$2[S^n\text{-}O] \rightarrow 2[S]^n + O_2\text{----------Eq.=4}$$

$$\text{Overall reaction} = 4OH^- \rightarrow O_2 + 4H_2O + 4e^-$$

Where [S] = the catalytically active site in the anodic catalyst and *n* = average oxidation state of the active site. It can be seen that the attachment of the hydroxyl group to the active site of the catalyst [S] initiates the OER process. This can be facilitated by the local oxidation of the metal center. It can be perceived from the above mechanism that the catalytic activity can be affected by any factor that can regulate the oxidation potential of the catalytically active surface site. By varying the local coordination environment of the metal site, the oxidation potential of the metal site can be varied [9,10]. Taking this aspect into consideration researchers moved from metals to metal oxides, metal oxyhydroxides, metal hydroxides, metal chalcogenides, metal phosphides, metal nitrides, metal borides, and so on, which will be discussed in the following sections.

## 1.4. TRANSITION METAL OXIDE OER CATALYSTS AND ADVANTAGES OF Ni AS THE CATALYTICALLY ACTIVE SITE

Electroactive catalysts are typically used to reduce the applied potentials to a lower value thereby bringing the overpotential (i.e. excess energy) as close as possible to the thermodynamic water splitting voltage. The most commonly used high-efficiency catalysts for this purpose are the precious metal oxides ($IrO_x$, $RuO_x$) which show some of the lowest overpotential for practical current densities [17-27].

Despite the efficiency exhibited by precious metal oxides for OER catalysis, the cost involved in employing them on a larger scale hinders them from being used for practical usage [28-41]. This stood as motivation for researchers to investigate earth abundant nonprecious metal catalysts (NPMCs) [42]. Earth abundant Ni –oxides, -oxyhydroxides, and –hydroxides among NPMCs, have shown catalytic performance comparable to that of precious metal oxides [28-41].

In order to understand why Ni-based electrocatalysts show superior activity, several theoretical and experimental studies were carried out and the outcome was the learning that this can be attributed to various factors including the band alignment and occupancy of the *d*-levels of the transition metal [43-45]. It has been predicted that an $e_g$ occupancy of $1e^-$ helps the catalytic activity of the transition metal center [17]. It has been observed that the most influential factor to predict and optimize catalyst efficiency was the above molecular orbital descriptor [17, 23] According to the studies corresponding to the molecular orbital descriptor, Co(II) based systems with a low spin octahedral coordination for Co should produce the best water oxidation catalyst. Actually, organometallic complexes of Co does show high catalytic performance which has been researched extensively by many groups [46-50].

In reality, as opposed to the expectations, Ni-based oxides and hydroxides which have a $t_{2g}^6 e_g^2$ electronic configuration for octahedral $Ni^{2+}$, outperform the Co-based oxides/hydroxides in terms of the potential required for oxygen evolution. It was observed after several experimental studies that NiOOH species which is formed in situ by oxidation of $Ni^{2+}$ to $Ni^{3+}$ preceding the water oxidation reaction. In the linear current-voltage scan, Ni oxidation from $Ni^{2+}$ to $Ni^{3+}$ shows up as a pre-peak before the actual water oxidation process. $Ni^{3+}$ achieves $e_g^1$ electronic configuration retaining the octahedral coordination, which explains the high catalytic activity of the NiOOH. Some recently discovered non-oxidic electrocatalysts have outperformed oxide based catalysts opening new directions of research [51-55].

## 1.5. NON OXIDIC OER ELECTROCATALYSTS AND EFFECT OF COVALENCY

Through different theoretical and experimental studies, it has been observed that the catalytic activity is dependent on the *d*-electron occupancy, especially the half-filled $e_g$ offered better catalytic activities [17]. It was also observed that increasing covalency in the metal-oxygen bond led to better catalytic efficiency in oxide based catalysts.

Based on the sound chemical intuition of changing the local environment around the transition metal atom in the lattice and replacing the oxide coordination sphere with chalcogenide coordination sphere leading to the change in redox potential of the atom, Nath research group pursued studies on Metal Sulfides, Selenides and Tellurides. For a specific metal ion, the covalency increases with increasing anion size and since the chalcogenides are bigger than the oxides according to that of Fajan's rule, it can be expected that metal-chalcogen bonds will have a greater degree of covalent character than

the metal oxides [56]. Over the last couple of years, Nath group has synthesized some of the first selenide based OER catalysts, $Ni_3Se_2$ [51,52], $NiSe_2$ [53] , $Co_7Se_8$ [54], $Cu_2Se$ [55], $Ni_3Te_2$ as well as mixed metal selenides, $NiFe_2Se_4$, $FeNi_2Se_4$, $NiCo_2Se_4$, $Ni_xAl_yFe_zSe_n$ [55] which has shown better catalytic activities than the other reported electrocatalysts till date as shown in the Figure.1.4.

Detailed electrochemical characterization has shown that the $Ni^{2+} \rightarrow Ni^{3+}$ oxidation potential in a seleno-based coordination environment is lower than that found in oxides, making available $Ni^{3+}$ at a lower potential in the selenide [51-55]. This will lead to the lowering of the overpotential needed for OER in selenides when compared to that of oxides.

This fact has been supported by results obtained from analysis of pure, single crystals of a seleno-based molecular complex containing $NiSe_4$ tetrahedral core [57] and selenide based thin films [54].

It is to be noted that the former is quite important since these complexes are stable coordination complexes with no tendency to form surface oxides proving the intrinsic catalytic activity of the $NiSe_4$ unit and changing the coordination from oxide to selenide can indeed increase catalytic activity.

Recently, OER activity of $Ni_3Te_2$ was obtained as shown in the Figure 1.5. An overpotential of 170mV at $10mAcm^{-2}$ was obtained and compared to that of $NiO_x$, $Ni_3S_2$ and $Ni_3Se_2$ in Table 1.2. Supporting the hypothesis of increasing covalency resulting in improved catalytic activity, $Ni_3Te_2$ showed a lower overpotential compared to that of $Ni_3S_2$ and $Ni_3Se_2$. This same trend of reduction in overpotential was also observed for the Co- and Cu-based chalcogenides [Table 1.2]. Decreasing electronegativity from S to Te

suggests increasing degree of covalency in the metal-chalcogen bond. These results formed a strong basis for this work.

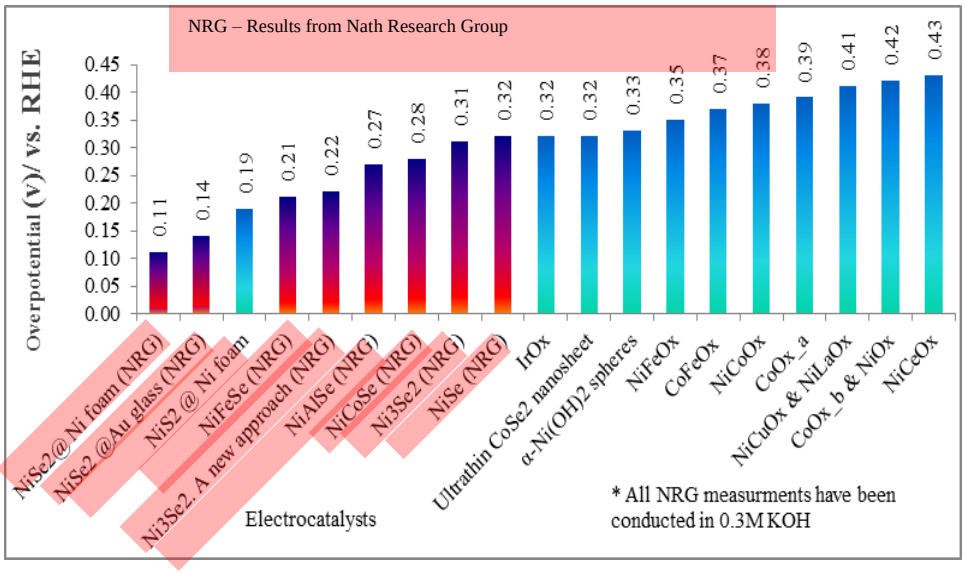


Figure 1.4. Comparison of selenide based OER electrocatalyst reported by the Nath group with conventional oxides.

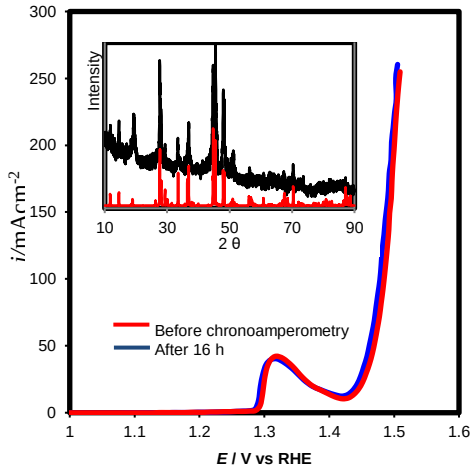


Figure 1.5. Electrocatalytic activity of $Ni_3Te_2$ deposited on carbon cloth. Red and blue curves correspond to activity before and after 16 h of chronoamperometry, respectively. Inset shows powder X-ray diffraction of the film (black) compared with $Ni_3Te_2$ standard (red).

Table 1.2.: Comparison of overpotential at 10 mA/cm$^2$ between oxide and chalcogenides.

| | Oxide | Sulfide | Selenide | Telluride |
|---|---|---|---|---|
| Ni | 330 mV ($NiO_x$) | 310 mV ($Ni_3S_2$) | 210 mV ($Ni_3Se_2$) | 170 mV ($Ni_3Te_2$) |
| Co | 411 mV ($Co_3O_4$) | 361 mV (CoS/Ti) | 260 mV ($Co_7Se_8$)[5] | - |
| Cu | 450 mV (Cu/CuO) | 420 mV ($Cu_2S$) | 320 mV ($Cu_2Se$) | - |

## 1.6. RATIONAL DESIGN OF A HIGH-EFFICIENCY ELECTROCATALYST

Based on the above discussion one can design a high performance OER catalyst which meets the following criteria [6].

1) The electrocatalyst should possess a low intrinsic overpotential for the oxygen evolution reaction.
    - Increased covalency in the anionic network (Section 1.8.)
2) The electrocatalyst should have a high active surface which facilitates both good accessibility to the reactants (electrolyte and $OH^-$ ions) and sufficiently fast removal of products such as gases, liquids and ions.
    - Nanostructuring (Section 1.9)
3) The electrocatalyst should possess a high electrical conductivity to provide pathways for electrons. If the electrocatalyst is not a good electrical conductor, it increases the resistance in the circuit leading to poor performance.

- Use of reduced graphene oxide (Section 1.11)

4) The electrocatalyst should be compatible with the electrolyte. Alkaline fuel cells have electrolytes with pH varying from 13 to 14. The catalytic material should not lose its chemical stability when exposed to such harsh alkaline conditions.
    - Chemical robustness (Section 3 of paper - chronoamperometry)
5) The electrocatalyst should be electrochemically stable and not corrode at high overpotentials.
6) The electrocatalyst should possess good mechanical and thermal stability for high temperature electrolysis.
    - Structural integrity (covalent solids)
7) The electrocatalyst should be of low cost for commercial applicability in the long run.
    - Using earth abundant transition earth metals (Section 1.4)

In this thesis we have investigated the OER catalytic activity of a novel transition metal boride, $Ni_3B$ and $Ni_3B$-rGO which has been designed and predicted to have high activity based on the hypothesis claimed in Section 1.7. and the effect of lattice covalency as has been described above.

## 1.7. POSSIBLE ADVANTAGE OF USING BORIDES

Proposed Hypothesis: This hypothesis is proposed based on observations from the previous studies that was discussed in the previous sections. 1) Presence of boron (B) around the Ni-atom provides a more covalent network which might enhance catalytic activity; 2) B being an electron deficient Lewis acid [56] may also facilitate attachment of

the anionic ($OH^-$) group (Lewis base) thereby enhancing catalyst activation [56]; 3) Structural Richness (different chemical compositions) of the transition metal borides, makes it an interesting family of compounds to get fundamental understanding of the structure property correlation. This work involves the study of $Ni_3B$ and $Ni_3B$-rGO as electrocatalysts for OER. The reason behind choosing Ni as the cation for OER catalysis in this work has been discussed in Section 1.4. The reason behind choosing $Ni_3B$ and rGO as a reinforcement for better electrical conductivity in this work has been explained in the following sections.

## 1.8. STRUCTURE OF $Ni_3B$ AND BOND COVALENCY OBSERVED IN THE M-B BOND AND REASON FOR SELECTION OF TRANSITION METAL BORIDES

$Ni_3B$ has a cementite like structure ($Fe_3C$) in the orthorhombic space group Pnma with four formula units (Z = 4) per unit cell, where eight metal atoms (M(g)) are in general positions (8d), four metal atoms (M(s)) in special positions (4c) and four nonmetal atoms (X) in the interstices [58]. In $Ni_3B$, Ni is situated in the centers of 15 vertices polyhedra, while B atoms are located in 3 capped trigonal prisms formed by Ni as shown in Figure 1.6. below [59]. The shortest interatomic distances in Ni—B at 2.0337 Å, Ni—Ni at 2.4538 Å are in good agreement with the sum of atomic radii of the elements (r(Ni) = 1.25 Å and r(B)=0.83 Å [60].

The stability of $M_3X$ compounds involves two competitive processes: (i) a loss in metal–metal bond strength due to the volume expansion caused by the addition of carbon or boron in the interstitial positions of the metal lattice, and (ii) an energy gain due to favorable bonding interactions of metals with these nonmetal atoms. The equilibrium cell

volumes of the borides (i.e. the metal–metal distances) are large considering the atomic radii of boron (0.91 Å) as shown in Table 1.3.

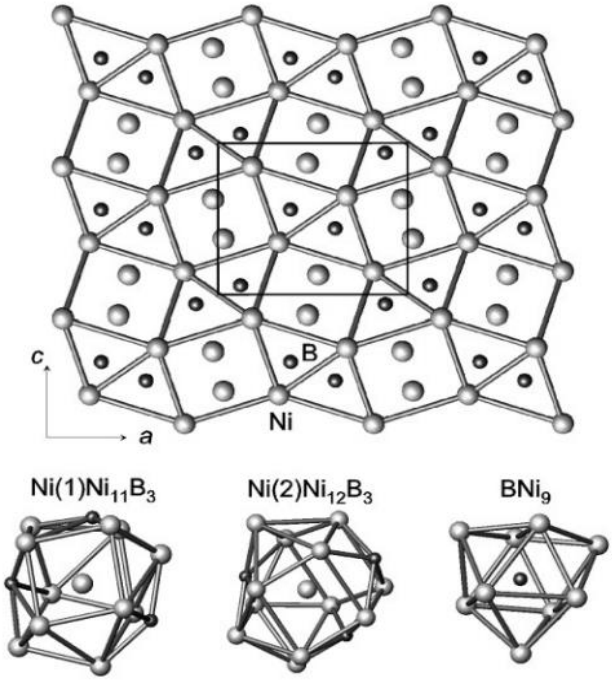


Figure 1.6. Structure of $Ni_3B$ representing the bonding between Ni-Ni and B occupying interstitial position. [58]

Table 1.3. The optimized lattice parameters (a,b and c, in Å), cell volumes ( $V^o$ in $Å^3$) and atomic coordinates for $M_3X$, Cementite phases. [58]

| **Phase** | **$Fe_3C$** | **$Co_3C$** | **$Ni_3C$** |
|---|---|---|---|
| **A** | 5.058(5.082) | 4.946(5.077) | 4.956 |
| **b** | 6.703(6.733) | 6.698(6.727) | 6.809 |
| **c** | 4.506(4.521) | 4.427(4.516) | 4.465 |
| **M(g)** | 0.1766;0.0678;0.3326 | 0.1806;0.0594;0.3296 | 0.1735;0.0733;0.3214 |
| **M(s)** | 0.0362;0.25;0.8360 | 0.0399;0.25;0.8424 | 0.0444;0.25;0.8349 |
| **X** | 0.8756;0.25;0.4402 | 0.8813;0.25;0.4453 | 0.8816;0.25;0.4450 |
| **$V_o$** | 152.77 | 146.66 | 150.67 |

Table 1.3. The optimized lattice parameters (a,b and c, in Å), cell volumes ( $V^o$ in $Å^3$) and atomic coordinates for $M_3X$, Cementite phases (cont.). [58]

| **Phase** | **$Fe_3B$** | **$Co_3B$** | **$Ni_3B$** |
|---|---|---|---|
| **A** | 5.397(5.433) | 5.145(5.221) | 5.199(5.2224) |
| **b** | 6.648(6.656) | 6.615(6.631) | 6.642(6.6165) |
| **c** | 4.368(4.454) | 4.405(4.408) | 4.388(4.3920) |
| **M(g)** | 0.1751;0.0556;0.3508 | 0.1841;0.0594;0.3496 | 0.1805;0.0629;0.3456 |
| **M(s)** | 0.0182;0.25;0.8832 | 0.0240;0.25;0.8659 | 0.0290;0.25;0.8663 |
| **X** | 0.8812;0.25;0.4268 | 0.8795;0.25;0.4387 | 0.8818;0.25;0.4380 |
| **$V_o$** | 156.70 | 149.90 | 151.55 |

The volume expansion of borides leads to the weakening of M–M bonds. Therefore, the stabilization of cementite-like borides is due to stronger covalent bonding in $M_3B$ phases because of considerable M–B bonds strengthening as compared with M–C bonds in the isostructural carbides [60].

The chemical bonding display in Figure 1.7. [58] the difference electron density ($\Delta\rho$) maps for $Fe_3C$, $Ni_3C$, $Fe_3B$ and $Ni_3B$ determined as $\Delta\rho = \{\rho_{cryst} - \Sigma\rho_{at}\}$, where $\rho_{cryst}$ and $\rho_{at}$ are the valence electron densities for the cementite-like phases and the corresponding free atoms.

In the case of $Ni_3B$, $\Delta\rho$ along the B–M lines increases, and the formation of Ni–B bonds including both nickel atoms in general as well as in special positions are observed.

The electron densities demonstrate that the cementite-like borides have a stronger covalent bonding than carbides due to the hybridization of boron and metal states—as it was found also in the density of states [58].

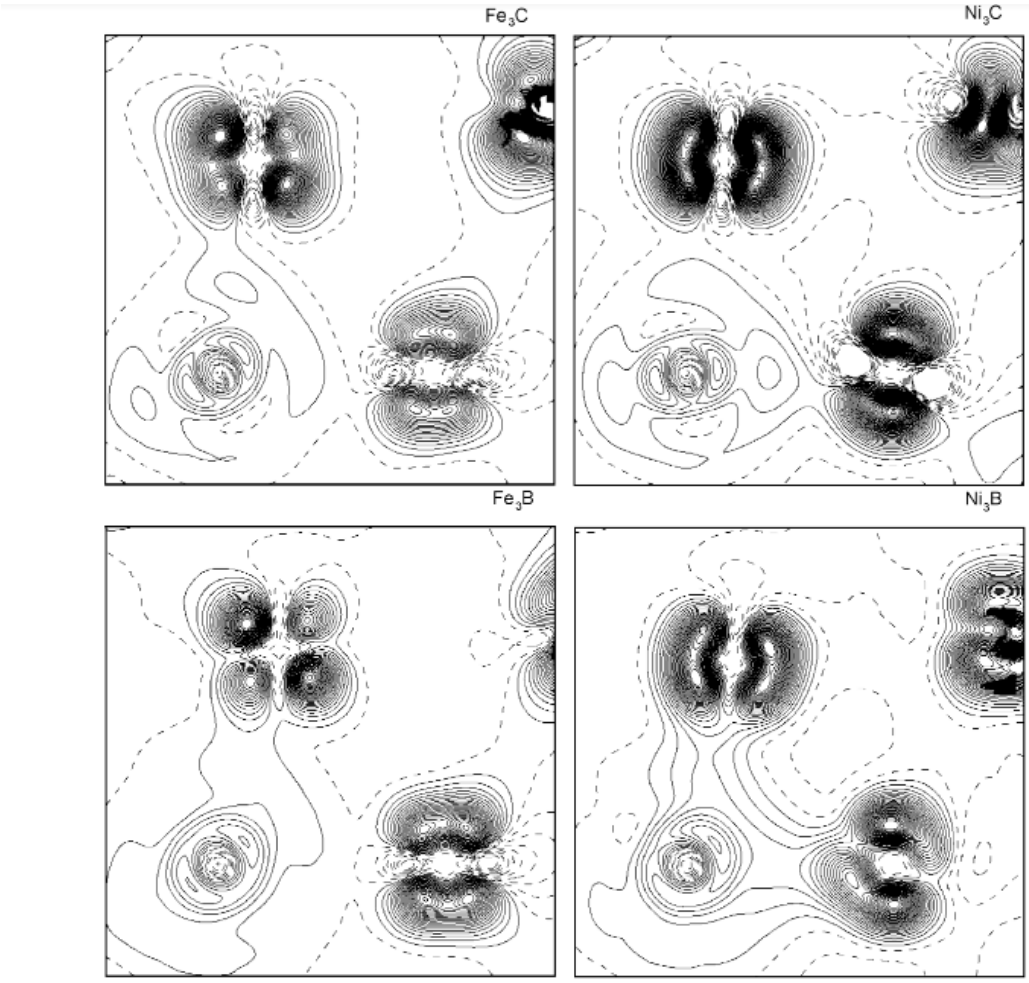


Figure 1.7.: The difference electron density ($\Delta\rho$) maps for $Fe_3C$, $Fe_3B$, $Ni_3C$ and $Ni_3B$ in planes having M(g)-X-M(s) bonding atoms. Dashed lines indicate $-\Delta\rho$ values. [58]

This is the reason (i.e considerable degree of bond covalency observed in Ni-B bond) behind choosing $Ni_3B$ for studying electrocatalytic activity. All cementite-like borides are stable phases due to stronger M–B hybridization [58].

Metal is the catalytically active site and $Ni_3B$ is a metal rich boron compound [61]. The electrical properties of $Ni_3B$ was also analyzed to enhance its catalytic performance by making a composite of itself with reduced graphene oxide, an electrically conductive matrix.

Reduced graphene oxide was chosen as a reinforcement to improve the electrical conductivity of the catalytic material.

Electrical conductivity is an important property, an electrocatalytic material should possess as explained in Section 1.6. The reason for choosing reduced graphene oxide has been explained in Section 1.11.

The electrical conductivity of $Ni_3B$ single crystals in three main crystallographic directions was found to be $0.0625*10^8$ S/m, $0.0264*10^8$ S/m and $0.0552*10^8$ S/m in [100], [010] and [001] respectively and it was concluded that $Ni_3B$ is a brittle metallic conductor with pronounced anisotropic properties [62].

This work involves the study of polycrystalline $Ni_3B$ powder and no single crystals of $Ni_3B$. The electrical conductivity of $Ni_3B$ power based thick film conductors was found to be $11.6 * 10^{-3}$ S/m for $0.30 m^2/g$, specific surface area of the powder [63]. A question might arise as to why to go for transition metal borides, despite having several well performing electrocatalysts as discussed in the previous sections on non-oxidic electrocatalysts.

Transition metal borides have been receiving attention in the last two decades for applications in aerospace and high temperature processes. Metal borides have low density and low coefficient of thermal expansion, which is desirable for aerospace applications demanding low strength to weight ratio [64] to reduce cost.

Some of these borides are also ceramic materials which possess melting points beyond $3000^oC$, and typically referred to as ultrahigh temperature ceramics (UHTCs). The thermal and mechanical properties of certain UHTCs are shown in Table 1.4. [65] below.

Table 1.4. Mechanical and thermal properties of UHTCs. [65]

| **Material (Crystal Struc. =Hex)** | **Melting Point (°C)** | **Density (g $cm^{-3}$)** | **Co-efficient of thermal expansion ($\alpha$;$10^{-6}$ $K^{-1}$)** | **Thermal Conductivity ($Wm^{-1}K^{-1}$)** | **Elastic Modulus (GPa)** | **Hardness (GPa)** | **Fracture toughness (MPa $m^{1/2}$)** |
|---|---|---|---|---|---|---|---|
| $TiB_2$ | 3225 | 4.5 | 7.4 | 60-120 | 560 | 25-35 | 4-5 |
| $HfB_2$ | 3380 | 11.2 | 6.3 | 104 | 480 | 28 | 4 |
| $ZrB_2$ | 3200 | 6.1 | 6.8 | 60-105 | 350 | 20-25 | 4 |
| $TaB_2$ | 3040 | 12.5 | 8.2 | 16-35 | 550 | 25 | 4.5 |

These ceramic borides, owing to their temperature-robustness, will be very useful for applications in steam pyrolysis and high temperature fuel cells. However, borides have not been investigated extensively for water electrolysis or related experiments for energy conversion from sustainable resources. Hence in an attempt to initiate boride based electrocatalysts for energy conversion processes, nickel boride ($Ni_3B$) nanostructures were analyzed to study the electrochemical performance in harsh alkaline conditions. The incorporation of boron increases the oxidation resistance of Ni [66]. The idea was to understand the mechanism and expand the concept to other Ni-doped UHTCs for electrolysis of water/steam.

## 1.9. NANOSTRUCTURING FOR OER ELECTROCATALYST

Nanostructuring of the catalyst is very important in increasing the catalytic efficiency for OER. Currently many researchers work on reducing the particle size of the materials, thereby increasing the surface area of the electrocatalysts [67-70]. Several authors have reported the synthesis of $IrO_2$ nanoparticles with particle sizes varying down

to approximately 1.6 nm. [67-70]. This approach has effectively increased the number of surface atoms with respect to bulk thereby increasing the OER activity of the catalyst. A major issue that is caused due to this approach is that it becomes difficult to establish structure−activity relationships for the OER due to the complex nature of the surface species, which are difficult to examine experimentally. With respect to the applied potential, the surface of the catalyst changes under the electrocatalytic conditions and thus the in situ techniques such as in situ XPS or XAS are extremely important in establishing a structure−activity−stability relationships. The effect of particular preferential formation of *OH species on high surface area $IrO_2$ [71] leading to enhanced OER activity is noticeable in spherical nanoparticles. $Co_3O_4$ has noticeably good performance as an OER electrocatalyst [72, 73, 74-104] but only 1/1000 of the exposed sites are practically responsible for the electrocatalytic activity of $Co_3O_4$. In the case of $Co_3O_4$, the surface active sites change by varying the overpotential. The surface structure acted quite dynamic and to improve the OER performance amorphization of the reactive surface was carried out to form the required intermediates [105]. Increase in the surface area of $Co_3O_4$, directly increases the number of active sites. Different phases of nickel sulfides have been tested as potential electrocatalysts for OER [106, 107, 108] and noticeably, superior performance was observed in some nanostructured nickel sulfides [109]. Certain cobalt sulfides have good electrochemical properties for ORR [110-113], but their performance is not as good for OER [114, 115, 116]. Researchers are trying to reduce the OER overpotential to make cobalt sulfide a bifunctional electrocatalyst [117]. An electrochemically deposited film of cobalt sulfide nanosheets reported by Liu et al. could conduct OER with an overpotential of 361 mV at 10 $mA/cm^2$ with stable

electrocatalytic activity for at least 20 h [118]. This performance has been attributed to the increased performance observed with respect to nanostructuring the material. The electrocatalytic activity of $CoSe_2$ in bulk form is poor and its structure was exfoliated to expose electroactive Co sites for OER. The superior electrocatalytic activity of $CoSe_2$ nanosheets was attributed to the presence of surface active sites [119]. The electrocatalytic activity of high surface area porous nickel phosphide is higher towards OER when compared to that of bulk nickel phosphide, also exhibiting a superior activity for HER in acidic media [120]. The observation of increased surface area leading to exposure of more electrocatalytically active surface sites led to this work nanostructuring the electrocatalyst to improve the catalytic performance.

## 1.10. REVIEW OF SYNTHESIS OF $Ni_3B$ NANOSTRUCTURES

Several synthesis procedures were reported for $Ni_3B$ microstructures and nanostructures. Amorphous Ni−B alloys were deposited on various substrates through vapor-liquid-solid mechanism from $NiCl_2$ and decaborane/pentaborane as reductants and the boron sources [121]. These films were further annealed at 800°C to produced $Ni_3B$ micro particles. Metal borides are limitedly considered for hydro desulfidization (HDS) [122-126]. Skrabalak et al. studied using HDS over unsupported crystalline $Ni_3B$ and $Co_2B$ [124]. These phases were obtained by annealing at 450 °C in oxygenated water. The resulting particles had a diameter of 100 nm approximately. The assessment of the presence of amorphous boron oxide was not done. The authors showed that these phases were unstable in harsh HDS conditions (450 °C) and were readily sulfided and converted into the corresponding metal sulfides, which are typical HDS catalysts.

Use of organic solvents at atmospheric pressure most often leads to the formation of amorphous metal borides because the temperature range that can be reached in such conditions is not sufficient to trigger crystallization. Synthesis of nano scaled amorphous metal boride relies on the procedures as those developed for aqueous synthesis involving the reduction of metal salts by borohydride. Since the 1950s, aqueous and organic procedures have been continuously developed in parallel when Co−B [127] and Fe−B [128] systems were obtained in diethyl ether, followed by Ni−B [129] and Co−Ni−B [130] systems in ethanol. A process involving the organic solvent based reduction was reported to produce aggregated $Ni_3B$ particles with a diameter of 50−90 nm. The solvent used was tetra-ethylene glycol with a boiling point of 280 °C and the reductant/boron source was potassium borohydride in excess of the nickel source (19:1 $KBH_4$ : $NiCl_2{\cdot}6H2O$). Aggregates of amorphous nanoparticles were formed at 100 °C and then crystallized to $Ni_3B$ upon further heating up to 280 °C. Crystallization is accompanied by the smoothing of particle surfaces due to Oswald ripening [131]. For Co−B alloys, the B content reaches values ranging from 25 to 40 atom % [132-135] a composition close to $Co_2B$. A reaction of $2CoCl_2$ (aq) + $4NaBH_4$ (aq) + $9H_2O$(l) →$Co_2B$(s) + 4NaCl(aq) + 12.5H (g)+ $3B(OH)_3$ (aq) was proposed by Glavee et al. and co-workers in anaerobic conditions. Considering the above literature, $NiCl_2{\cdot}6H_2O$ was used as the nickel precursor and anhydrous sodium borohydride, $NaBH_4$ was used as the boron source in this work to synthesize $Ni_3B$ and the reaction was carried out in aqueous media. The experimental procedure to synthesize $Ni_3B$ has been discussed in Section 2 of paper. Diglyme was used as the chelating agent for slow release of Ni in the chemical reaction.

## 1.11. REDUCED GRAPHENE OXIDE AS A REINFORCEMENT FOR IMPROVED ELECTROCATALYTIC ACTIVITY

Various types of carbon are widely used in the realm of electrochemistry as conventional electrodes. Although their overpotentials for OER are high, it is still reasonable to use carbon as a metal-free electrode for OER due to low cost and versatility in design [136-145]. The best example is the chemical interaction of nitrogen-doped carbon with active metal oxides [146, 147]. It has been reported that spreading a network of hexagonal carbon on the substrate electrode provides a better pattern for the deposition of the electroactive material. When using a graphene sheet over the substrate electrode, the growth of the electroactive material can be considered to form a better structure in favor of OER [148, 149]. In many works, various types of carbon nanomaterials such as graphene and reduced graphene oxide [74, 82, 86, 92, 96, 112, 117, 136, 142, 144, 148-187] have been used to build a nanocomposite with the electrocatalyst. This improves the electrical conductivity between the electrocatalyst particles while increasing the specific surface area of the electrode. However, this is not usually a simple mechanical mixture of two or more solids. Instead, there are chemical interactions between the carbon and the electrocatalyst through the carbon functional groups. Reduced graphene oxide has properties between graphene and graphene oxide [188]. Delocalization of the π electrons over the conjugate 2D network of $sp^2$ hybridized carbon is the reason for high electrical conductivity observed in reduced graphene oxide [189,190]. Even though delocalization of the π electrons is observed in reduced graphene oxide, it is not as good electrical conductor as that of graphene. This is due to the presence of attached functional groups and defects in the conjugate 2D network caused due to the involved synthesis procedure [188]. The reason behind researchers still pursuing research on reduced graphene oxide

as opposed to that of the better graphene is due to the complexity involved in the synthesis of graphene [191]. Use of reduced graphene oxide enables a better electron transfer from the catalyst surface to the electrode due to the delocalization of the $\pi$ electrons. Electron transfer between the catalyst and the substrate holding the catalyst is facilitated by reduced graphene oxide [147, 148, 150-158, 161-163, 165, 166, 168, 169, 170, 173, 174, 175, 178, 192]. Due to this phenomenon of better charge transfer, an improvement in the catalytic performance is observed [147, 148, 150-158, 161-163, 165, 166, 168, 169, 170, 173, 174, 175, 178, 192]. This has been observed in several studies. For example, $Co_3O_4$ nanocrystals on graphene reported by Hongjie et al. has shown an improvement in the catalytic activity for OER compared to that of $Co_3O_4$ itself by synergistic effect observed in catalyst due to the addition of reduced graphene oxide. [187]. This has been shown in the Figure 1.8 below. The linear sweep voltammetric (LSV) scan shown in Figure 1.8 a) shows the comparison of OER and ORR activity of $Co_3O_4$ by itself and $Co_3O_4$/N-rmGO (Nitrogen doped reduced graphene oxide). LSV is plotted with applied voltage against the current density observed. This plot is used to determine the overpotential for OER and onset potential for OER. Taking a closer look at OER LSV scan, it can be observed that $Co_3O_4$/N-rmGO shows a better catalytic activity as compared to that of $Co_3O_4$. This can be understood by the cathodic shift of the LSV curve of $Co_3O_4$ towards the thermodynamic water splitting voltage of 1.23V vs RHE after the addition of N-rmGO. The OER LSV comparison of $Co_3O_4$, $Co_3O_4$-rmGO (rmGO=reduced graphene oxide), $Co_3O_4$-NrmGO can be found in Figure 1.8 b). $Co_3O_4$ shows an overpotential of 345mV at 10mA/cm$^2$. A lower overpotential of 320mV at 10mA/cm$^2$ is observed in the case of $Co_3O_4$-rmGO due to the addition of reduced

graphene oxide. The Tafel plot is used to understand the kinetics of the reaction. Lower Tafel slope implies better charge transfer in the system. It can be observed in Figure 1.8 c) that $Co_3O_4$-rmGO has a lower slope as compared to that of $Co_3O_4$ itself.

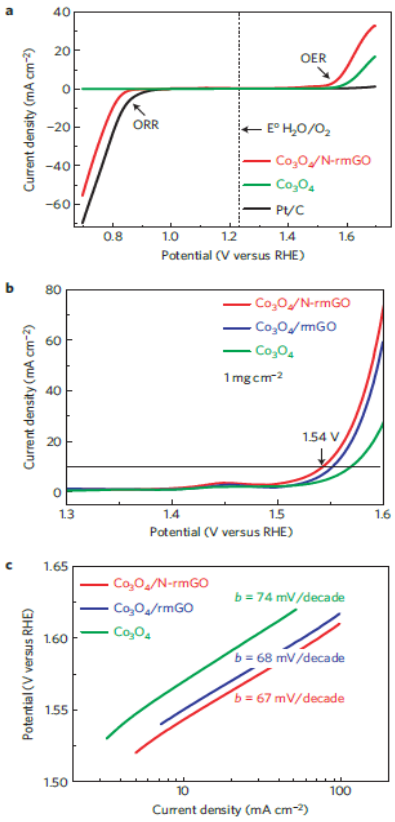


Figure 1.8. Comparison of a) OER and ORR performance of Pt, $Co_3O_4$ & $Co_3O_4$/N-rmGO in $O_2$ saturated 0.1M KOH. b) LSV of $Co_3O_4$, $Co_3O_4$/rmGO & $Co_3O_4$/N-rmGO. c) Tafel curve of $Co_3O_4$, $Co_3O_4$/rmGO & $Co_3O_4$/N-rmGO. [187]

Another case can be considered involving the addition of Nitrogen doped reduced graphene oxide (N-rGO) to Mn and Co substituted $Fe_3O_4$ (MCF) that was reported [193]. The LSV curve in Figure 1.9. a) shows that N-rGO by itself is not even able to provide a current density of 10mA/cm$^2$ with application of the voltage up to 1.9V vs RHE. MCF by itself is achieving a current density of 10mA/cm$^2$ at 1.8V vs RHE. When a hybrid catalyst

of MCF/N-rGO (black curve) is made, an increase in the catalytic performance is observed with 10mA/cm$^2$ current density observed at an applied potential of 1.7V. This performance was attributed to the better charge transfer observed between the electrode and catalyst surface through nitrogen doped reduced graphene oxide. The electrical conductivity of reduced graphene oxide produced by reducing graphene oxide with hydrazine hydrate was found to be 2000 S/m [189].

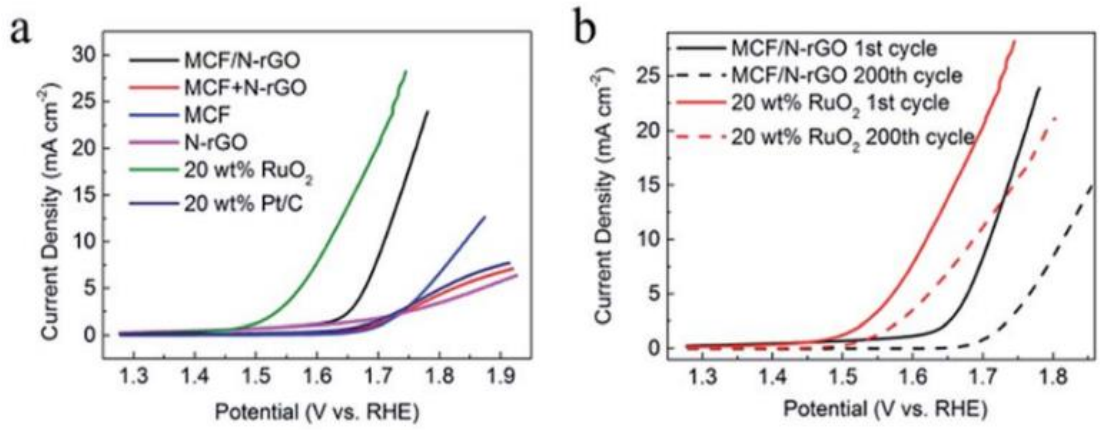


Figure 1.9. The electrochemical measurements have been performed in $O_2$ saturated 0.1M KOH. (a) LSV curves depicting the improvement of performance with incorporation of N-rGO to MCF. (b) MCF/N-rGO and $RuO_2$ subjected to 200 cycles of LSV. [193]

A composite of less electrically conductive $Ni_3B$ as mentioned in Section 1.8 with a more conductive reduced graphene oxide was made to improve the catalytic performance of the material.

# 2. METHODS OF CHARACTERIZATION

The catalyst synthesized in this work has been characterized using the following methods.

Powder X-ray diffraction (PXRD)**:-** The synthesized catalyst was characterized through powder X-ray diffraction using Philips X-Pert using Cu Kα (1.5418 Å) radiation. The PXRD pattern was collected from 5° to 90°.

Transmission Electron Microscopy (TEM):- High resolution TEM images and selected area electron diffraction (SAED) were obtained using FEI Tecnai F20. The probe current is 1.2 nA with a spot size of less than 2 nm. STEM mode in the TEM was also used for dark field imaging where the convergence angle was 13 mrad and the camera length was 30 mm. This scope is equipped using an Oxford ultra-thin (UTW) window energy dispersive X-ray spectroscopy (EDS) detector, which allows detection of the elements.

X-ray photoelectron spectroscopy (XPS):- XPS measurements of the catalysts were performed using a Kratos Axis 165 X-ray Photoelectron Spectrometer using the five monochromatic Al X-ray source. The spectra were collected as is without sputtering with Ar for 30 sec which removes approximately >1 nm from the surface.

Scanning Electron Microscopy (SEM):- SEM images of the catalyst were obtained from Hitachi S-4700 at an acceleration voltage of 15KV using the secondary electron detector. The scope is equipped with EDAX genesis EDS system.

# 3. PRODUCT DEVELOPMENT

## 3.1. FUNCTIONAL FABRICS FOR WATER SPLITTING

To make electrocatalysts available for consumer applications, the second direction of research is aimed at developing a catalyst ink that can be coated on cotton fabrics and polyester fabrics as catalyst stacks for applications in fuel cells.

## 3.2. COTTON AND POLYESTER FABRIC BASED ELECTRODES FOR ALKALINE FUEL CELLS

Many abundantly available natural materials were assessed for production of electrode stacks. Cotton is an abundantly available perennial crop which is extensively used in making fabrics (39% of the world's fabrics) [194].

Polyester is a fiber that is also widely used in making fabrics. Extensive amount of research is going on in producing economically feasible biodegradable aliphatic polyester that does not result in pollution.

Polyhyroxybutarate (PHB) and Polylactic acid (PLA) are the most extensively studied biodegradable thermoplastic polyesters. Both are a truly biodegradable and biocompatible and both have a relatively high melting point (160 to 180 °C). [195].

Cotton fabrics are stable in harsh alkaline conditions [196] but contain non-conductive cellulose network. Cotton has been made conductive by coating it with a carbon based conductive suspension prepared by exfoliation through ultrasonication.

The procedure developed to make the cotton conductive has been discussed in the Section 3.5.

## 3.3. MOORE'S LAW FOR FIBERS

"Fabrics that see, hear, sense, communicate, store and convert energy, regulate temperature, monitor health and change color – heralding the dawn of a Fabric Revolution." – Advanced Functional Fabrics of America (AFFOA).

## 3.4. PROGRESSION TOWARDS THE PRODUCTION OF FUNCTIONAL FABRICS

AFFOA published a roadmap [197] on the development of functional fabrics over the next 5 years, where energy storing apparel has a place in 2021 as shown in Figure 3.1. below. This gives the confirmation and motivation that this work is not a mere chase of a superfluous dream.

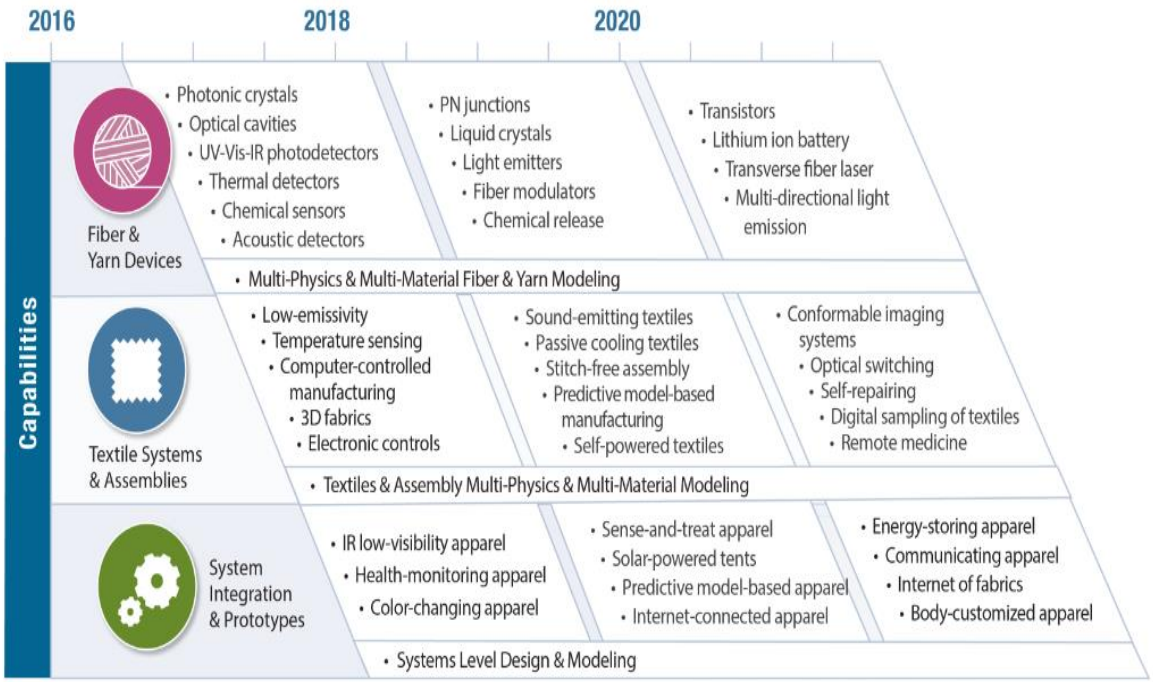


Figure 3.1. AFFOA Roadmap. [197]

## 3.5. CATALYST INK PREPARATION

0.5g of graphite was ultrasonicated in 5ml of N,N dimethylformamide for 36 hours. After sonication the solution was left undisturbed for three days. The supernatant was separated by centrifugation at 12000 RPM. The supernatant remained black even after centrifugation. The supernatant is expected to be a graphene suspension produced by exfoliation of graphite.

## 3.6. ELECTROCHEMICAL ANALYSIS

Cotton was dipped in the ink and dried at $145^0$C for five times and analyzed in a three electrode system with reference electrode as calomel electrode and counter electrode as platinum mesh in 1MKOH.

## 3.7. PRELIMINARY RESULTS

OER performance of the catalyst ink coated cotton was analyzed and the results are as shown in the Figure 3.2. below.

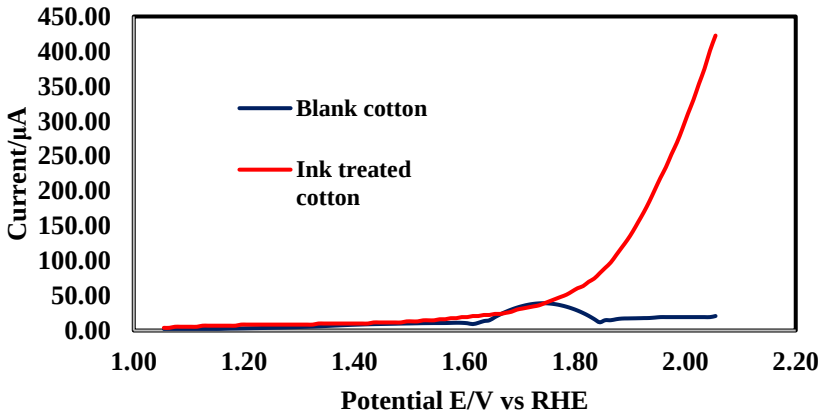


Figure 3.2. Comparison of OER performance of blank cotton and ink treated cotton

## 3.8. FUTURE WORK

The ink suspension obtained from the above procedure is not very viscous. Better adhesion of the ink can be achieved by increasing the viscosity of the ink. So, polyaniline, a conductive polymer will be added to the suspension to increase the viscosity. After producing a conductive viscous ink, electrocatalytically active metal chalcogenides or metal borides will be added to the suspension.

## PAPER

# FACILE SYNTHESIS OF $Ni_3B$/RGO NANOCOMPOSITE AS AN EFFICIENT ELECTROCATALYST FOR OXYGEN EVOLUTION REACTION IN ALKALINE MEDIA

Maalavan Arivu[a], Jahangir Masud[b], Siddesh Umapathi[b], and Manashi Nath[b]*

[a]Materials Science & Engineering, Missouri University of Science & Technology, Rolla, MO 65409, USA.
[b]Department of Chemistry, Missouri University of Science & Technology, Rolla, MO 65409, USA.

*Email: nathm@mst.edu

## ABSTRACT

Alkaline water electrolysis yielding $H_2$ and $O_2$ is a very promising fuel cell technology for sustainable energy generation. The emphasis has been placed on development of efficient electrocatalysts comprising of earth-abundant elements, for the kinetically deterrent oxygen evolution reaction (OER). Nickel boride nanostructures exhibit enhanced OER catalytic activity achieving 10 mA $cm^{-2}$ at overpotential of 340 mV. The activity can be greatly improved by incorporating $Ni_3B$ in electrically conductive reduced graphene oxide matrix bringing the overpotential further down to 290mV at 10 mA $cm^{-2}$ along with a small Tafel slope. The catalytic activity of $Ni_3B$-rGO nanocomposite show extensive stability under long term operational condition.

Keywords: Water splitting, OER electrocatalysts, reduced graphene oxide, Nickel borides, Synergistic effect.

# 1. INTRODUCTION

Electrocatalytic water splitting to produce $H_2$ and $O_2$ is one of the most promising research direction for clean energy generation. However, the sluggish kinetics of oxygen evolution reaction (OER) poses hindrance in the path of effective and efficient water splitting which requires high energy to break the activation barrier [1]. Thus, efforts have been devoted to explore the efficient electrocatalysts for OER. $RuO_2$ and $IrO_2$ have been identified to be efficient OER catalysts [2]. However, these precious metal oxides are not feasible for large scale $O_2$ production due to the scarcity and cost associated with these precious metals [3, 4]. Additionally, these noble metal oxides also suffer from long term instability in strong alkaline conditions [5]. Earth abundant transition metal oxides, hydroxides and oxy-hydroxides have recently been used to replace precious metal oxides as electrocatalysts for OER in alkaline medium [6-7]. Recently, earth abundant transition metal chalcogenides have proved to be better than oxides due to lesser anion electronegativity and compatible electronic structure [8-12]. Metal borides and metal phosphides are the latest addition to the family of electrocatalysts for water splitting [13-18]. For example, $Co_2B$ [13] and $FeB_2$ [14] have recently been reported to catalyze the overall water splitting reaction at low overpotentials. More recently, $Ni_xB$ nanosheets have shown high catalytic efficiency for OER [15] and amorphous Ni-B [16] alloy has shown a high efficiency for hydrogen evolution reaction (HER) over a broad pH range.

Electrocatalysis is enabled by fast faradaic redox reactions that happen at electrolyte-electrode interface [19]. This phenomena that happens at the surface can be made more efficient by increasing the surface area of the catalyst thereby exposing more

active sites [20]. Nanostructuring of the catalyst, not only increases the surface area but also as a consequence exposes the catalytically active sites. Besides nanostructuring, the catalyst activity can be significantly improved by making a composite with reduce graphene oxide (rGO) [21]. Part of this enhancement is due to the increased conductivity of the rGO matrix which helps electron transport in the within the catalyst composite.

Herein we have reported $Ni_3B$/rGO nanocomposite as highly efficient OER electrocatalyst. The $Ni_3B$-rGO hybrid nanocomposite was synthesized by solution based reaction. The nanocomposite catalyst requires only 290 mV overpotential vs RHE to achieve 10 mA $cm^{-2}$ OER current density with a small Tafel slope (88.4 mV/dec). Interestingly, the $Ni_3B$-rGO nanocomposite shows very high stability for $O_2$ evolution over extended period of time.

# 2. MATERIALS AND METHODS

Synthesis of $Ni_3B$ nanostructure**:** 1mmol of $NiCl_2$ was dissolved in 5ml of bis (2-methoxyethyl) ether and stirred until a yellowish green solution was obtained. The prepared solution was then dissolved in 200ml deionized water. Then, 10 mmol of dry $NaBH_4$ was added dropwise, whereby, a black precipitate was formed immediately. The solution was stirred for one hour. At the completion of the stirring period, the black precipitate was separated by centrifugation and washed several times with ethanol and deionized water. Finally, the product was dried in vacuum oven at room temperature for overnight. The possible reaction of $Ni_3B$ synthesis is presented below:

$$6\ NiCl_2 + 12\ NaBH_4 + 30\ H_2O = 2\ Ni_3B + 12\ NaCl + 39\ H_2 + 10\ H_3BO_3$$

Synthesis of nickel boride/rGO nanocomposite**:** Graphene oxide (GO) was prepared by modified hummers method [22]. 0.5 ml of hydrazine hydrate was added to GO (1:1 wt. % of catalyst) dispersed in 5ml of deionized water and heated at 70 ºC for two hours. Synthesized rGO was mixed with dry $NaBH_4$ and the same procedure for synthesizing nickel boride nanostructures was carried out to produce the hybrid nanocomposite.

Electrode preparation**:** 2 mg of the catalyst was added to 100µL of 2% Nafion solution and was ultrasonicated for 20mins leading to formation of a catalyst ink. 10µL of this solution was drop-casted on carbon finer paper (CFP) and air dried to be later used as the anode.

Electrochemical study: The OER activity was performed by linear sweep voltammetry (LSV) and the stability of the catalyst was obtained from chronoamperometry at constant potential using conventional three electrode electrochemical cell. Standard calomel electrode (SCE), Pt mesh and $Ni_3B/Ni_3B$-rGO films on CFP were used as reference, counter and working electrodes, respectively. All potentials obtained in this study (*vs* SCE) were converted to the reversible hydrogen electrode (RHE) by using the following equation.

$$E_{RHE} = E_{SCE} + 0.059\ pH + E^0_{SCE} \quad (1)$$

Where $E_{RHE}$ is the converted potential *vs* RHE, $E_{SCE}$ is the experimentally measured potential *vs* SCE, and $E^0_{SCE}$ is the standard thermodynamic potential of SCE at 25 °C (0.242 V).

The electrocatalytic activity and kinetics of an electrochemical process can be explained by Tafel equation [23] as follows:

$$\alpha_a = \left(\frac{RT}{nF}\right)\left(\frac{dlnj_a}{dE}\right) \quad (2)$$

where $\alpha_a$ is anodic transfer coefficient, n is number of electron involved in the reaction, F is Faraday constant and $j_a$ is the current density, and Tafel slope is given by ($dlnj_a/dE$).

The turnover frequency (TOF) is an important parameter that quantifies the specific activity of a catalytic site for OER reaction under defined reaction conditions by the number of catalytic cycles occurring at the active center per unit time.

$$\mathrm{TOF} = \frac{I}{4 \times F \times m} \quad (3)$$

where I is the current in Amperes, F is the Faraday constant and m is the number of moles of the active catalyst.

# 3. RESULTS AND DISCUSSIONS

PXRD patterns of $Ni_3B$ and $Ni_3B$-rGO composite along with $Ni_3B$ standard pattern (PDF # 01-082-1699) are shown in Figure. 3.1. Both of the experimental pxrd patterns confirmed the presence of $Ni_3B$. However, the peal intensities were fairly low and exhibit a broad peak between 37º to 57º suggesting that the product was weakly crystalline phase. Broadening of the diffraction peaks can be attributed to the small grain sizes of the catalyst

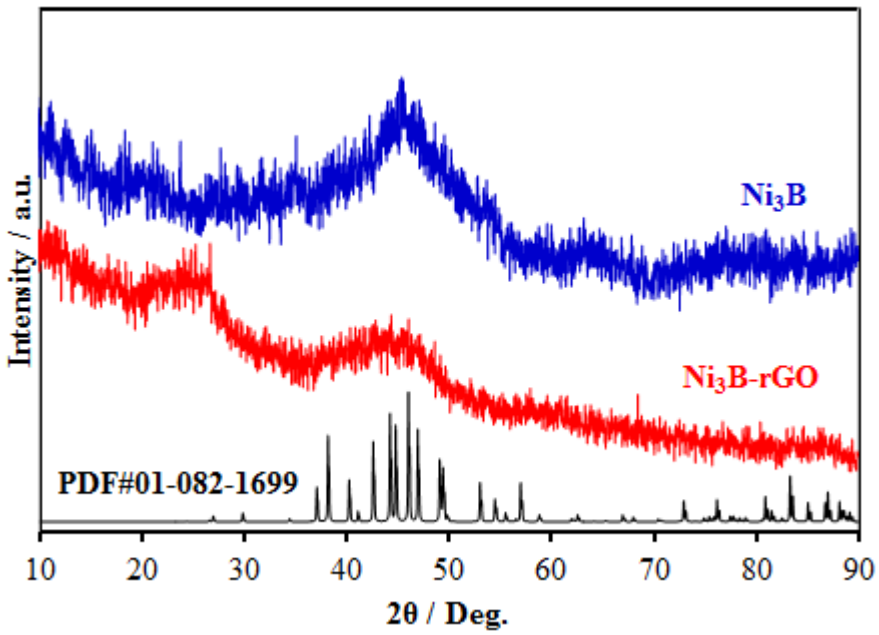


Figure 3.1. PXRD patterns of $Ni_3B$ and $Ni_3B$-rGO compared with the reference (PDF # 01-082-1699).

nanoparticles. SEM images of the $Ni_3B$ (Figure. 3.2a) and $Ni_3B$-rGO (Figure. 3.2d) nanocomposite showed that the product was mainly composed of well-dispersed spherical nanoparticles. Particle size distribution was analyzed from several SEM images and insets in Figure 3.2a and Figure 3.2d show histograms for particle size distributions

of $Ni_3B$ and $Ni_3B$-rGO nanocomposite, respectively. Particle size distribution of $Ni_3B$-rGO was found to be relatively smaller 30–55 nm (average 42 nm) than $Ni_3B$, 45-70 nm (average 57 nm). Smaller particle size along with the synergistic effect of rGO might be attributed the better catalytic activity of the hybrid nanocomposite.

TEM analysis of $Ni_3B$ and $Ni_3B$-rGO nanocomposite as shown in Figures. 3.2b and 3.2e, respectively confirmed the presence of randomly distributed catalyst nanoparticles. SAED patterns obtained from $Ni_3B$ (inset of Figure. 3.2b) and $Ni_3B$-rGO

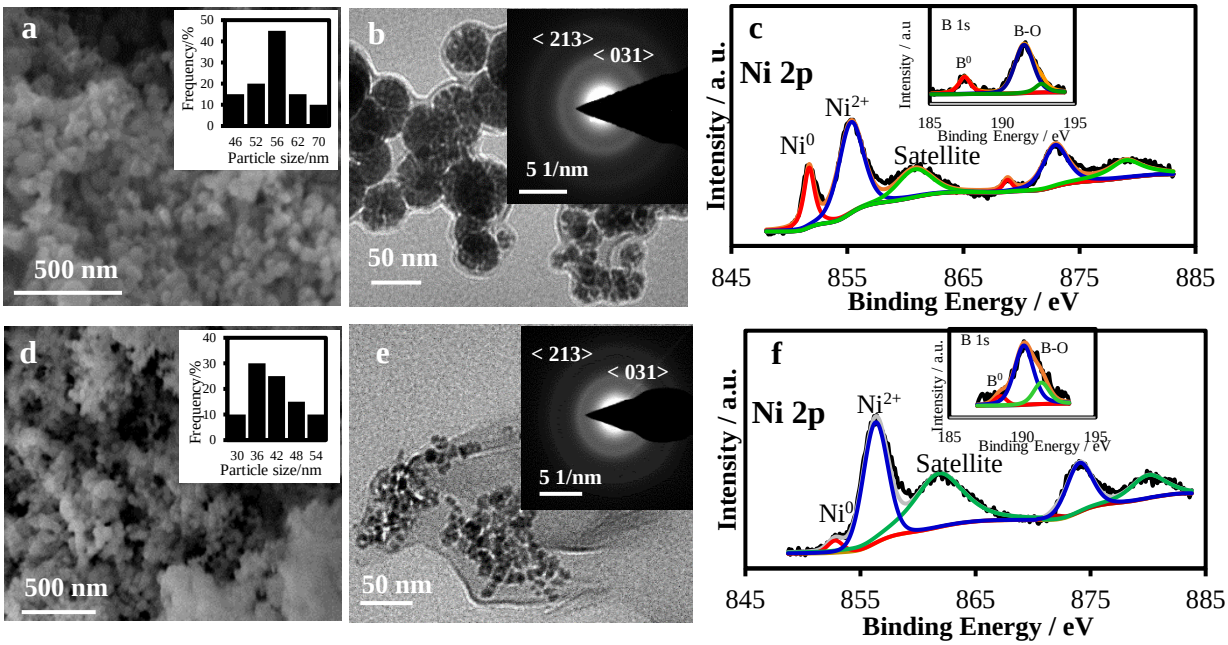


Figure. 3.2 (a) – (c) Analysis of $Ni_3B$ catalyst. (a) SEM image with inset showing histogram of particle size distribution. (b) TEM image with inset showing the SAED pattern. (c) Ni 2p and B 1s (inset) XPS spectra. (d) – (f) Characterization of $Ni_3B$-rGO nanocomposite. (d) SEM image, inset showing histogram of particle size distribution. (e) TEM image inset showing the SAED pattern. (f) Ni 2p and B 1s (inset) XPS spectra.

(inset of Figure.3.2e) showed similar diffuse diffraction rings corresponding to <213>, and <031> lattice planes of $Ni_3B$, which also confirmed the presence of $Ni_3B$ phase in the catalysts.

X-ray photoelectron spectroscopy (XPS) was employed to investigate the oxidation states of Ni and B in $Ni_3B$ (Figure 3.2c) and $Ni_3B$-rGO (Figure 3.2f) catalysts. Three distinct peaks of the Ni $2p_{3/2}$ core levels was observed for both $Ni_3B$ and $Ni_3B$-rGO. The peak at the low binding energy of ca. 852eV can be assigned to metallic $Ni^0$ [19] originating from the core level of $Ni_3B$ nanoparticles as expected for nickel borides [24-25]. The 2nd peak at about 855.5 eV of both catalysts is close to $Ni^{2+}$ signal and the third peak at higher binding energy correspond to the satellite peak due to the overlapping of antibonding orbitals. Insets of Figure 3.2c and Figure3.2f show B1s spectra from both samples. The peak at 188.0 eV can be assigned to the $B^0$ signal in $Ni_3B$ [24-25]. It should be noted that the binding energy of B 1s in $Ni_3B$ is higher than the amorphous elemental boron (187.3 eV) [26], indicating electron cloud shifted towards the Ni from B. The peak at higher binding energy can be attributed to surface boron oxides [24-25].

The OER activity of $Ni_3B$ and $Ni_3B$-rGO was measured in $N_2$ saturated 1 M KOH with a scan rate of 10 mV $s^{-1}$ using linear sweep voltammetry (LSV) and the results were compared with $RuO_2$ (Figure 3.3a). LSVs of rGO and carbon fiber paper (CFP) were also measured for reference. It can be observed that CFP did not show any OER activity and on the other hand, rGO by itself showed very less OER activity. However, modification of CFP with $Ni_3B$, and $Ni_3B$-rGO showed excellent OER activity as can be seen in Figure. 3.3a. The onset potential for $O_2$ evolution was at 1.51 V *vs* RHE for $Ni_3B$ and an overpotential (η) of 340 mV was required to achieve 10 mA $cm^{-2}$ current density.

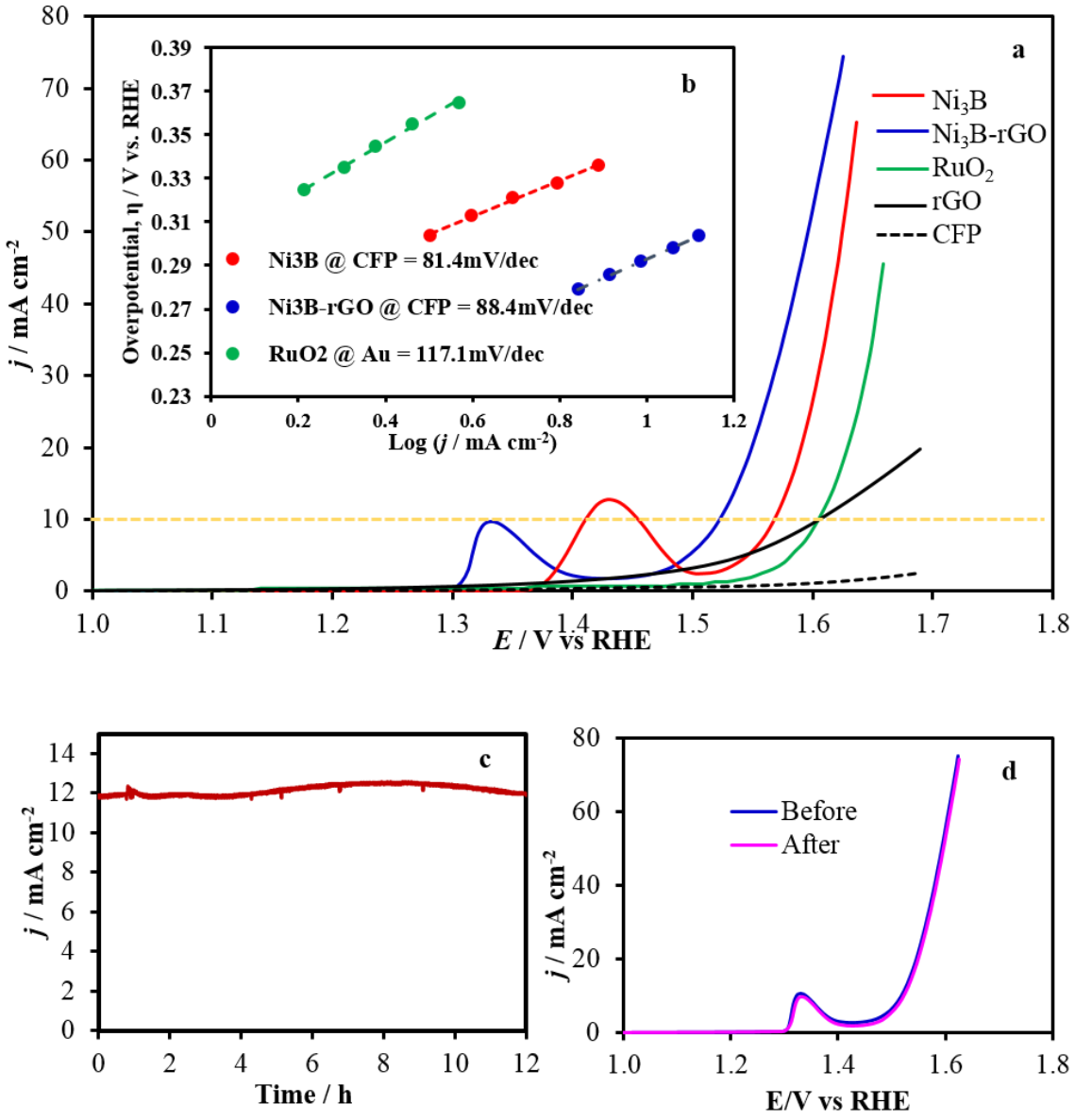


Figure 3.3 **(**a) LSVs measured for different catalysts coated on CFP substrate in $N_2$ saturated 1.0 M KOH solution at a scan rate of 10 mV $s^{-1}$. (b) Tafel plots of catalysts. (c) Chronoamperometric study for $Ni_3B$-rGO nanocomposite at a potential of 1.52 V vs. RHE for 12 h in 1 M KOH. (d) Comparison of catalytic activity before and after chronoamperometry for 12 h.

Interestingly, when $Ni_3B$ was modified with rGO the onset potential and η at 10 mA $cm^{-2}$ was further lowered to 1.43 V *vs* RHE and 290 mV at of 10 mA $cm^{-2}$, respectively. This excellent OER activity can be attributed the synergistic effect in the

catalyst-rGO composite which facilitates charge transfer within the catalyst matrix in presence of rGO during the catalytic process [27]. Another interesting observation is that the Ni-oxidation peak that is typically observed due to catalyst activation and creation of $Ni^{3+}$ also occurs at more cathodic potential in $Ni_3B$-rGO compared to $Ni_3B$. This can also be attributed to the synergistic effect due to the presence of rGO matrix, which can facilitate the $Ni^{2+}$ oxidation at lower potential than $Ni_3B$. Previously we have shown that catalyst activation at lower potential leads to lower onset potential for OER. These OER activities were compared with $RuO_2$ which shows an onset potential and η at 10 mA $cm^{-2}$ current density at 1.51 V *vs* RHE and 370 mV, respectively, which are comparable with previous reports [26]. It should be noted here that $Ni_3B$-rGO nanocomposite showed much higher catalytic activity (low onset potential and η) amongst the reported boride based OER electrocatalysts (Table 3.1).

The kinetics for OER were investigated by analyzing the Tafel plots as shown in Figure. 3.3b. Tafel slopes were obtained as 81.4 mV $dec^{-1}$, 88.4 mV $dec^{-1}$ and 117.1 mV $dec^{-1}$ for $Ni_3B$, $Ni_3B$-rGO and $RuO_2$, respectively. Lower values of Tafel slope confirms better kinetics and higher catalytic activity of nickel borides. The turnover frequency of $Ni_3B$ and $Ni_3B$-rGO nanocomposite were calculated at an overpotential of 290 mV, assuming that all of the metal ions in the catalysts are catalytically active for OER. The TOF values were calculated to be 0.001 $s^{-1}$ and 0.012 $s^{-1}$ for $Ni_3B$ and $Ni_3B$-rGO, respectively. The higher TOF value of $Ni_3B$-rGO indicates better OER performance over $Ni_3B$, confirming the synergistic effect of rGO.

Table 3.1: A comparison of OER activity of different boride-based electrocatalysts

| Catalysts | Electrolyte | Onset potential / vs. RHE | Ƞ to get 10 mA $cm^{-2}$ / mV | Tafel slop / mV $dec^{-1}$ | References |
|---|---|---|---|---|---|
| $Co_2B$/NG | 0.1M KOH | 1.51 | 360 | 45 | 13 |
| $FeB_2$ | 1M KOH | 1.48 | 296 | 52.4 | 14 |
| $Ni_xB$ | 1M KOH | 1.54 | 380 | 89 | 15 |
| Nickel(II) Borate @ $Ni_3B$ | 1M KOH | 1.48 | 302 | 52 | 24 |
| Co-3Mo-B | 1M NaOH | 1.50 | 320 | 155 | 28 |
| $Ni_3B$ | 1M KOH | 1.51 | 340 | 81.4 | This work |
| $Ni_3B$-rGO | 1M KOH | 1.43 | 290 | 88.4 | This work |

Stability of the $Ni_3B$-rGO nanocomposite under operational condition was investigated by chronoamperometry whereby the potential was held constant at 1.52 V to achieve 10 mA $cm^{-2}$ for extended period of time (12h) in 1M KOH solution. It was observed that the current density did not show any degradation even after 12 h of continuous oxygen generation (Figure 3.3c) indicating exceptional durability and functional stability of the catalyst in alkaline medium. The OER polarization curves before and after chronoamperometry were also compared to check the catalyst stability (Figure 3.3d). Interestingly, the LSVs before and after 12 h or chronoamperometry were perfectly superimposable and the catalyst showed similar onset potential and overpotential at 10 mA $cm^{-2}$.

## 4. CONCLUSION

One step simple solution-based technique was used to synthesize $Ni_3B$ and $Ni_3B$-rGO nanocomposite, which showed highly efficient OER catalytic activity in alkaline medium. Among these $Ni_3B$-rGO nanocomposite showed exceptional electrocatalytic activity with low overpotential (290 mV) to achieve 10 mA $cm^{-2}$, which is one of the lowest overpotentials that has been reported for boride-based catalysts so far. The nanocomposite catalyst also exhibited a small Tafel slope 88.4 mV $dec^{-1}$ indicating faster reaction kinetics. The synergistic coupling between rGO and $Ni_3B$ nanoparticles is believed to be the driving force for the excellent OER activity.

## ACKNOWLEDGMENT

This work was supported by the American Chemical Society, Petroleum Research Fund [54793-ND10], and CASB, Missouri S&T. The authors would like to acknowledge Materials Research Centre for equipment usage.

# BIBLIOGRAPHY


[1] F. M. Sapountzi, J. M. Gracia, C.J. (Kees-Jan) Weststrate, H.O.A. Fredriksson, J.W. (Hans) Niemantsverdriet , Electrocatalysts for the generation of hydrogen, oxygen and synthesis gas, Progress in Energy and Combustion Science 58 (2017) 1–35.

[2] T. Reier, M. Oezaslam, P. Strasser, Electrocatalytic Oxygen Evolution Reaction (OER) on Ru, Ir, and Pt Catalysts: A Comparative Study of Nanoparticles and Bulk Materials, ACS Catal. 2 (2012) 1765-1772.

[3] J.Y. Kim, K. H. Kim, H.K. Kim, K.B. Kim, Template-Free Synthesis of Ruthenium Oxide Nanotubes for High-Performance Electrochemical Capacitors, ACS Appl. Mater. Interfaces 7 (2015) 16686-16693.

[4] D. Payne, Iridium's impact, Nat. Chem.**8** (2016) 392.

[5] E. Fabbri, A. Habereder, K. Waltar, R. Kötz, T. J. Schmidt, Developments and perspectives of oxide-based catalysts for the oxygen evolution reaction, Catal. Sci. Technol. 4 (2014) 3800–3821.

[6] Y. Cheng, S.P. Jiang, Advances in electrocatalysts for oxygen evolution reaction of water electrolysis-from metal oxides to carbon nanotubes, Progress in Natural Sciences, Materials International 25 (2015) 545-553.

[7] M.S. Burke, L. J. Enman, A.S. Batchellor, S. Zou, S.W. Boettcher, Oxygen Evolution Reaction Electrocatalysis on Transition Metal Oxides and (Oxy)hydroxides: Activity Trends and Design Principles, Chem. Mater. 27 (2015) 7549−7558.

[8] A. T. Swesi, J. Masud, M. Nath, Nickel selenide as a high-efficiency catalyst for oxygen evolution reaction, Energy Environ. Sci. 9 (2016) 1771-1782.

[9] A. T. Swesi, J. Masud, W. P. R. Liyanage, S. Umapathi, E. Bohannon, J. Medvedeva, M. Nath, Textured $NiSe_2$ Film: Bifunctional Electrocatalyst for Full Water Splitting at Remarkably Low Overpotential with High Energy Efficiency, Sci Rep. 7 (2017) 2401.

[10] I. H. Kwak, H. S. Im, D. M. Jang, Y. W. Kim, K. Park, Y. R. Lim, E. H. Cha, J. Park, $CoSe_2$ and $NiSe_2$ nanocrystals as superior bifunctional catalysts for electrochemical and photoelectrochemical water splitting. ACS Appl. Mater. Interfaces 8 (2016), 5327−5334.

[11] J. Masud, A. T. Swesi, W. P. R. Liyanage, M. Nath, Cobalt Selenide Nanostructures: An Efficient Bifunctional Catalyst with High Current Density at Low Coverage, ACS Appl.Mater. Interfaces 8 (2016) 17292-17302.

[12] T. Liu, Y. Liang, Q. Liu, X. Sun, Y. He, A. M. Asiri, Electrodeposition of cobalt-sulfide nanosheets film as an efficient electrocatalyst for oxygen evolution reaction, Electrochem. Commun. 60 (2015) 92–96.

[13] J. Masa, P. Weide, D. Peeters, I.Sinev, W. Xia, Z. Sun, C. Somsen, M. Muhler, W. Schuhmann, Amorphous Cobalt Boride ($Co_2B$) as a Highly Efficient Nonprecious Catalyst for Electrochemical Water Splitting: Oxygen and Hydrogen Evolution, Adv. Energy. Mater. 6 (2016) 1502313.

[14] H. Li, P. Wen, Q. Li, C. Dun, J. Xing, C. Lu, S. Adhikari, L. Jiang, D.L. Carroll, S.M. Geyer, Earth-Abundant Iron Diboride ($FeB_2$) Nanoparticles as Highly Active Bifunctional Electrocatalysts for Overall Water Splitting, Adv. Energy Mater, 7 (2017) 1700513.

[15] J. Masa, I. Sinev, H. Mistry, E. Ventosa, M.D.L Mata, J. Ariol, M. Muhler, B. R. Cuenya, W. Schuhmann, Ultrathin High Surface Area Nickel Boride (Ni*x*B) Nanosheets as Highly Efficient Electrocatalyst for Oxygen Evolution, Adv. Energy Mater. 7 (2017) 1700381

[16] M. Zeng, H. Wang, C. Zhou, J. Wei, K. Qi, W. Wang, X. Bai, Nanostructured Amorphous Nickel Boride for High-Efficiency Electrocatalytic Hydrogen Evolution over a Broad pH Range, ChemCatChem 8 (2016) 708-712.

[17] J. Masud, S. Umapathi, N. Ashokan, M. Nath, Iron phosphide nanoparticles as an efficient electrocatalyst for the OER in alkaline solution, J. Mater. Chem. A 4 (2016) 9750-9754.

[18] S. Barwe, C. Andronescu, E. Vasile, J. Masa, W. Schuhmann Influence of Ni to Co ratio in mixed Co and Ni phosphides on their electrocatalytic oxygen evolution activity, Electrochem. Commun. 79 (2017) 41–45.

[19] M. Gorlin, P. Chernev, J. F. D. Araiyao, T. Reier, S. Dresp, B. Paul, R. Krahnert, H. Dau, P.Strasser, Oxygen Evolution Reaction Dynamics, Faradaic Charge Efficiency, and the Active Metal Redox States of Ni−Fe Oxide Water Splitting Electrocatalysts, J. Am. Chem. Soc. 138 (2016) 5603-5614.

[20] Y. Chen, K. Yang, B. Jiang, J. Li, M. Zeng, L. Fu., Emerging two-dimensional nanomaterials for electrochemical hydrogen evolution J. Mater. Chem. A 5 (2017) 8187-8208.

[21] L. Ye, Z. Wen, Reduced graphene oxide supporting hollow bimetallic phosphide nanoparticle hybrids for electrocatalytic oxygen evolution, Electrochem. Commun. 83 (2017) 85–89.

[22] D. C. Marcano, D. V. Kosynkin, J. M. Berlin, A. Sinitskii, Z. Sun, A. Slesarev, L. B. Alemany, W. Lu, J. M. Tour, Improved Synthesis of Graphene Oxide, ACS Nano, 4 (2010) 4806-4814.

[23] R. Guidelli, R. G. Compton, J. M. Feliu, E. Gileadi, J. Lipkowski, W. Schmickler, S. Trasatti, Defining the transfer coefficient in electrochemistry: An assessment (IUPAC Technical Report), Pure Appl. Chem. 86 (2014) 245–258.

[24] J. Jiang, M. Wang, W. Yan, X. Liu, J. Liu, J. Yang, L. Sun, Highly active and durable electrocatalytic water oxidation by a $NiB_{0.45}/NiO_x$ core-shell heterostructured nanoparticulate film, Nano Energy, 38 (2017) 175-184.

[25] W. J. Jiang, S. Niu, T. Tang, Q. H. Zhang, X. Z. Liu, Y. Zhang, Y. Y. Chen, J. H. Li, L. Gu, L. J. Wan, J. S. Hu, Crystallinity-Modulated Electrocatalytic Activity of a Nickel(II) Borate Thin Layer on $Ni_3B$for Efficient Water Oxidation, Angew.Chem. Int.Ed. 56 (2017) 6572–6577.

[26] D. N. Hendrickson, J. M. Hollander, W. L. Jolly, Core-Electron Binding Energies for Compounds of Boron, Carbon, and Chromium, Inorg. Chem. 9 (1970) 612.

[27] S. Umapathi, J. Masud, A. T. Swesi, M. Nath, $FeNi_2Se_4$–Reduced Graphene Oxide Nanocomposite: Enhancing Bifunctional Electrocatalytic Activity for Oxygen Evolution and Reduction through Synergistic Effects, Adv. Sustainable Syst. 1 (2017) 1700086.

[28] S. Guptaa, N. Patela, R. Fernandesa , S. Hanchatea , A. Miotellob , D.C. Kothari, Co-Mo-B Nanoparticles as a non-precious and efficient Bifunctional Electrocatalyst for Hydrogen and Oxygen Evolution, Electrochim. Acta 232 (2017) 64–71.

# SECTION

## 4. DISCUSSION OF RESULTS NOT INCLUDED IN THE PAPER

Chronoamperometry (chrono) for 12hrs was performed to check the stability of as prepared $Ni_3B$ as shown in Figure 4.1 a.

The applied potential was 1.58V vs RHE. Cyclic voltammograms (CV) before and after 12 hrs of chronoamperometry were performed as shown in the Figure 4.1 b. The current density corresponding to that of 1.58V vs RHE obtained from that of the CV before checking chrono is 16.6 $mA/cm^2$.

The current density response in the beginning of the chrono shows a lower current density of 8 $mA/cm^2$ as opposed to that of the expected 16.6 $mA/cm^2$. The reason of the increased current density at the end of 12hrs is expected to be due to the opening of pores in the polymer binder used in the preparation of the catalyst ink.

The pores that are formed are expected to be formed due to the electrochemical activation of the polymer binder due to the application of an electric potential over a prolonged period of 12 hrs.

In Figure 4b, the $Ni^{2+}$ oxidation to $Ni^{3+}$ peak is observed at 1.43V vs RHE in the CV obtained before chrono and an anodic shift to 1.45V vs RHE is observed in the CV obtained after chrono. This implies that there is a slight degradation in the performance of the catalyst after 12 hours of chrono.

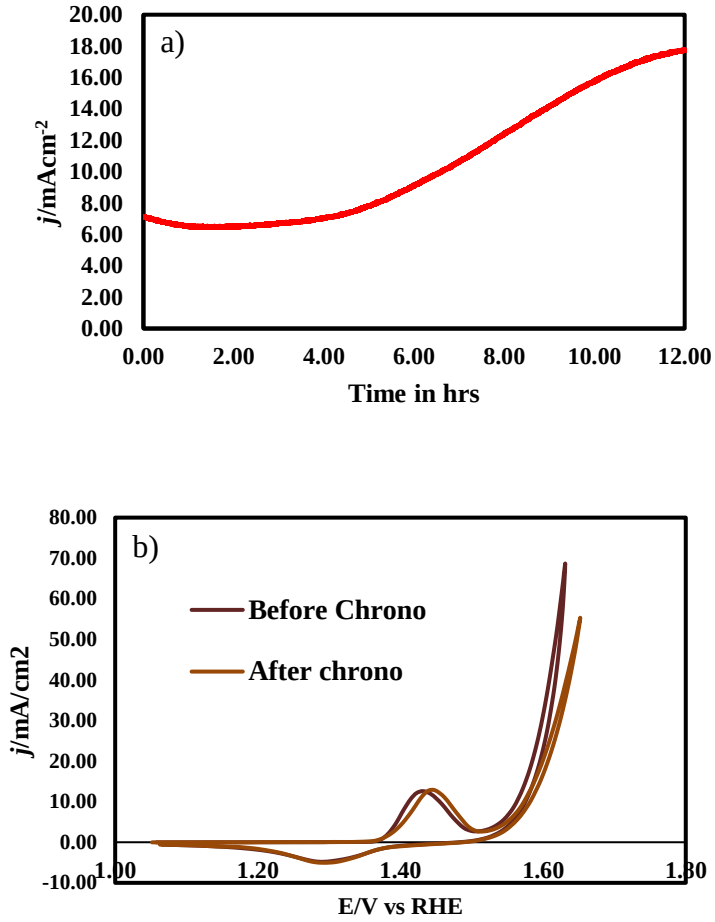


Figure 4.1 a) Chronoamperometric curve of $Ni_3B$ for 12hrs in 1M KOH. b) CV before and after chrono of $Ni_3B$.

C1s XPS spectra of $Ni_3B$ and $Ni_3B$-rGO is shown in the Figure 4.2 below. The C-C peak intensity increases in the case of $Ni_3B$-rGO as opposed to that of $Ni_3B$ proving that a composite between rGO and $Ni_3B$ is formed and the interaction is not just physical but also chemical [198].

The intensity of the broad peak containing C-O, C=O and O=C-OH in the case of both $Ni_3B$ nanostructures and $Ni_3B$-rGO nanocomposite have the same intensity.

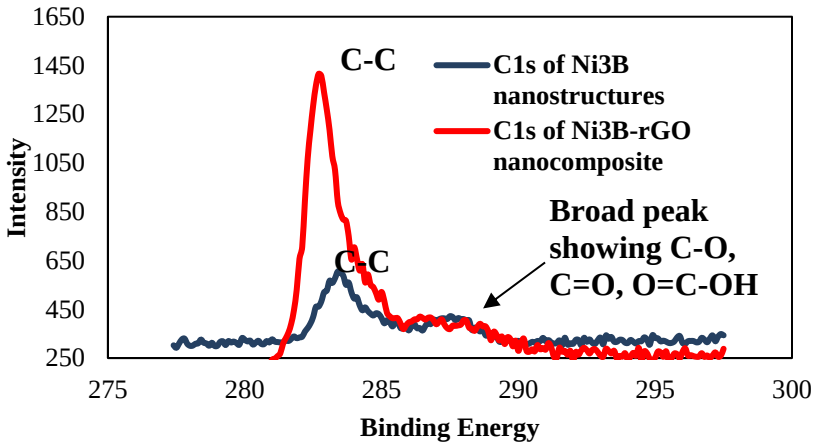


Figure 4.2. C1s XPS spectra of $Ni_3B$ and $Ni_3B$-rGO

TEM-EDS of $Ni_3B$ and $Ni_3B$-rGO were obtained as shown in the Figure 4.3 below. EDS scan of $Ni_3B$ in Figure 4.3a shows the presence of Ni and B. They exact composition of Ni and B obtained from that of EDS is not exact.

Since B signal at 0.12KeV closely matches with that of C signal, the exact composition cannot be obtained. The presence of C and Cu in the case of $Ni_3B$ is observed due to the layer of C present in the Cu grid used for sample preparation. TEM-EDS was carried out to determine the presence of any impurities.

It was found from the TEM-EDS scan of $Ni_3B$ that very little oxygen at 0.375KeV is present which can be attributed to that of the surface oxides present in the catalyst.

In the case of $Ni_3B$-rGO shown in Figure 4.3b, an increased intensity of C and O is found due to the presence of reduced graphene oxide. Boron peak is found to be coinciding with the carbon peak in Figure 4.3b giving an inaccurate atomic percentage of boron in EDS.

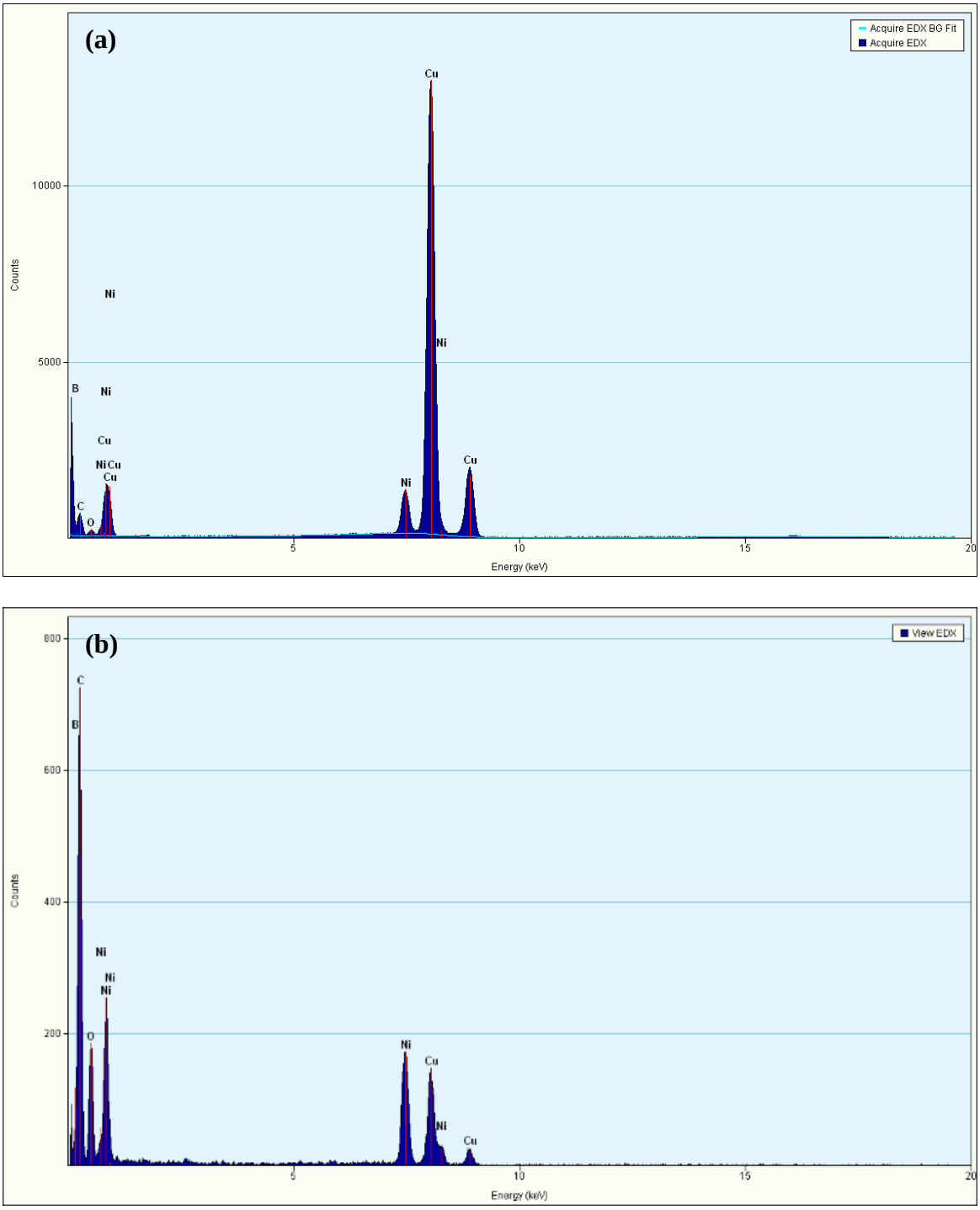


Figure 4.3. a) TEM-EDS scan of $Ni_3B$ and b) TEM-EDS scan of $Ni_3B$-rGO nanostructures.

$RuO_2$ was electrodeposited on gold substrate using 0.450g of $RuCl_3 \cdot H_2O$ and 2.98g KCl dissolved in an electrolyte of 0.01 M HCl by running 100 CVs from 0.06 to 0.96 V vs SCE at a scan rate of 0.05 V/s. Then the sample was annealed in air at 200 °C for 3 h [9]. $RuO_2$ was synthesized and checked for electrocatalytic activity to calibrate the electrochemical setup used for recording electrochemical measurements. $RuO_2$ is the state of the art electrocatalyst for OER. For a scan rate of 10mV/s, an overpotential of 380mV at $10mA/cm^2$ was observed matching with the results published by Jaramillo et al. [9].

Several Ni-based catalysts have been compared in the table below. The Ni-based catalyst have been arranged in the order of decreasing electronegativity of the anions upto $Ni_3Te_2$ and then the boride based nickel catalysts up to date have been presented. The trend observed going down from NiOx to $Ni_3Te_2$ is that with increasing bond covalency between the cation and anion and decreasing the electronegativity of the anion results in the lowering of the overpotential, implying a better catalytic performance. Metal borides are a new class of electrocatalytic materials researched upon for the bond covalency observed in the metal-boron bond. Telluride based compounds show a better catalytic performance than that of borides. The reason behind boron based compounds still being pursued is due to their superior mechanical properties and thermal properties, which makes them possible recruits for electrocatalyzing steam electrolysis. There are only three nickel based borides that have been reported for the electrocatalysis of OER as presented in the Table 4.1. The catalytic performance of the $Ni_3B$ and $Ni_3B$-rGO nanocomposite developed in this work has been mentioned in red in the Table 4.1. The performance of the catalyst developed in this work is comparable to that of the other

reported Ni-borides. Apart from the identification of $Ni_3B$ as an electrocatalyst for oxygen evolution reaction, the novelty of this work involves the addition of rGO to improve the catalytic performance of the catalyst which is enabled by better charge transfer between the electrolyte, catalyst and substrate. Apart from the comparison of the electrocatalyst developed in this work with other boride based electrocatalysts, the comparison with other reported Ni-based catalysts shows that the $Ni_3B$ and $Ni_3B$-rGO developed is comparable with the other reported catalysts.

Table 4.1: Comparison of Ni-based catalysts.

| **Electrocatalysts for water splitting** | **Electrolyte** | **Onset potential V** | **η @ 10 mA $cm^{-2}$ (mV *vs* RHE)** | **Reference** |
|---|---|---|---|---|
| $NiO_x$ nanoparticles[b] | 1M KOH | 1.52* | 331 | 199 |
| $NiO_x$/C | 1M KOH | 1.51* | 335 | 200 |
| Amorphous NiO | 1 M KOH | 1.54* | >470 [a] | 201 |
| α-$Ni(OH)_2$ | 0.1M KOH | 1.54* | 331 | 202 |
| $Ni(OH)_2$ /NiOOH | 1 M KOH | 1.80* | 525 | 203 |
| $Ni(OH)_2$ nanoparticles[b] | 1M KOH | 1.48* | 299 | 199 |
| $Ni_3S_2$–Ni foam | 0.1M KOH | 1.387 | 187 | 204 |
| $Ni_3S_2$–Ni foam | 1M NaOH | 1.46* | 260 | 205 |
| NiS/ Ni foam | 1 M KOH | 1.55 | 158[a] | 206 |

Table 4.1: Comparison of Ni-based catalysts (cont.).

| | | | | |
|---|---|---|---|---|
| $Ni_3Se_2$–Ni foam | 1M KOH | 1.48* | 270 [a] | 207 |
| $Ni_3Se_2$/Cu foam | 1M KOH | 1.51 | 343 [b] | 208 |
| $NiSe_2$ /Ti | 1 M KOH | 1.53* | 320 [c] | 209 |
| $NiSe_2$ | 1 M KOH | 1.43 | 250 | 210 |
| $NiSe_2$-DO | 1M KOH | 1.46* | 241 | 211 |
| $NiSe_2$ /Ti | 1M KOH | 1.53* | 295 [a] | 212 |
| $Ni_3Se_2$– Au Glass | 0.3 M KOH | 1.45 | 320 ±20 | 51 |
| $Ni_3Se_2$–Ni foam | | 1.46 | 270 ± 20 | |
| $Ni_3Se_2$ (30 s dissolution) @Au | 1M NaOH | 1.39 | 190 | 52 |
| NiSe nanowires | 1M KOH | 1.49* | 270[a] | 213 |
| $NiSe_2$ nanosheets | 1MKOH | 1.55 | 323 | 214 |
| $Ni_3Te_2$– Au Glass | 1M KOH | 1.38 | 210 [d] | 215 |
| $Ni_3Te_2$–Ni foam | | 1.45 | 230 [e] | |
| $Ni_3Te_2$– CFP | | 1.41 | 210 | |
| $Ni_3Te_2$– C Cloth | | 1.42 | 210 | |
| $Ni_3Te_2$– GC | | 1.36 | 180 | |

Table 4.1: Comparison of Ni-based catalysts (cont.).

| | | | | |
|---|---|---|---|---|
| $Ni_3Te_2$ - Hydrothermal | | 1.38 | 220 | |
| $Ni_xB$ | 1M KOH | 1.54 | 380 | 216 |
| Nickel (II) Borate @ $Ni_3B$ | 1M KOH | 1.48 | 302 | 217 |
| $Ni_3B$ | 1M KOH | 1.51 | 340 | This work |
| $Ni_3B$-rGO | | 1.43 | 290 | This work |

* Calculated from references; [a]@ 20 mA $cm^{-2}$; [b]@ 50 mA $cm^{-2}$; [c]@ 100 mA $cm^{-2}$,
[d] supplementary figure S3a , [e]supplementary figure S3b.

# 5. CONCLUSION

Electrocatalytic materials for OER are extensively investigated to lower the excess energy required for water oxidation. Metal in the electrocatalytic material is the active site for OER process to take place. Attachement of the hydroxyl ions to the catalytic site initiates the OER process. In this work, the local coordination environment around the metal center was varied to facilitate the attachment of $OH^-$. By introducing B around Ni in $Ni_3B$, a covalent network is established due to metal boron covalent interaction. This covalent interaction facilitated water oxidation in alkaline media making $Ni_3B$ a good electrocatalyst for OER. OER is an electron transfer reaction taking place between the electrolyte, catalyst and substrate holding the catalyst. Through literature review, it was found that reduced graphene oxide (rGO) by itself is not an active OER catalyst but when a hybrid of itself and the catalyst material is made, an increase in the catalytic performance is observed due to electron transfer from catalyst surface to the substrate. $Ni_3B$-rGO composite showed a better catalytic performance as compared to that of $Ni_3B$ due to better electron transfer.

# APPENDIX

## A.1. DETAILED DESCRIPTION OF ELECTROCHEMICAL METHODS

There are certain ways to analyze and bench mark the performance of a catalyst. A potentiostat is a device that is used to perform electrochemical analysis. Three electrode system consisting of the working electrode, counter electrode and the reference electrode was used to perform electrochemical analysis. The working electrode is the anode consisting of the electrocatalyst ink drop casted on carbon fiber paper. The counter electrode that was used is Platinum (Pt) mesh. Platinum does not interfere with the electrochemical reaction that take place at the anode and also simultaneously supports the hydrogen evolution reaction. The oxygen evolution reaction and hydrogen evolution reaction always coexist and cannot happen individually. Reference electrode that was used is the standard calomel electrode (SCE). All the electrochemical measurements were recorded with reference to the reference electrode. The potential scale can be moved based on convenience. So, the actual potential applied can be determined by altering the scale with respect to the reference.

**A.1.1. Linear Sweep Voltammetry (LSV).**This is the classic plot which is used to determine the overpotential. This is a plot between the voltage supplied versus current density. When the measurement is made with potentiostat, the current produced with respect to the voltage supplied is obtained. The current density is obtained by dividing the current with the catalyst area on the electrode. The plot appears to be as the one shown in the Figure A.1. below. The point where the non-faradaic region ends, marks the beginning of the oxygen evolution reaction. The potential at this point is called onset

potential. Lower onset potential implies that the electrocatalyst is an efficient OER catalyst. Overpotential is the potential at which, a current density of $10mA/cm^2$ is achieved.

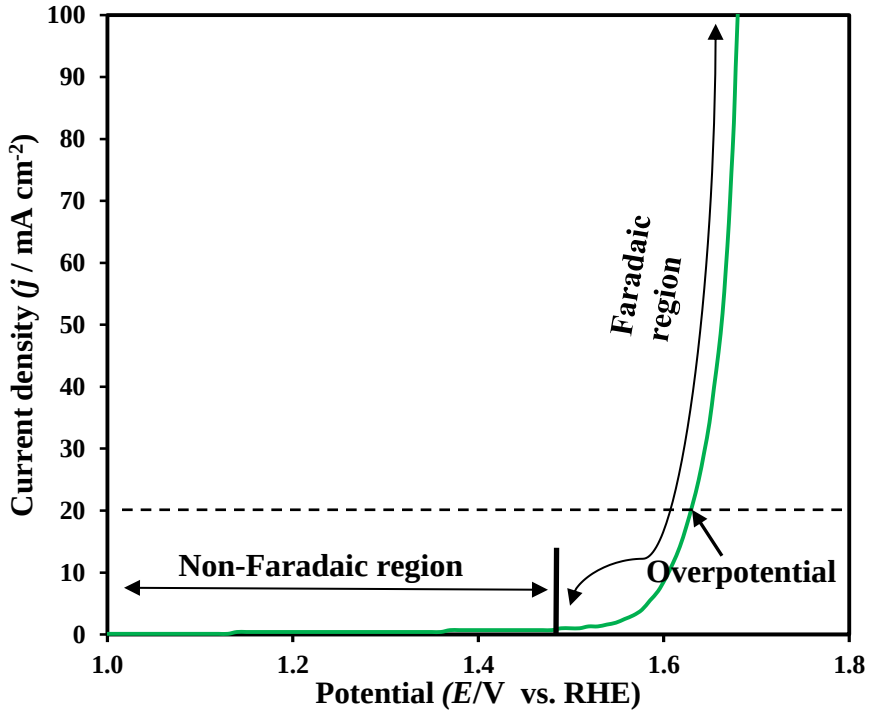


Figure A.1. Typical linear sweep voltammetric curve of oxygen evolution reaction. [218]

**A.1.2. Cyclic Voltammetry (CV).** Cyclic voltammetry gives the redox behavior of the material. CV is performed by cycling the potential of a working electrode and measuring the corresponding current response. The forward scan gives the information about oxygen evolution reaction and the reverse scan gives the information about oxygen reduction reaction. Typical CV plot is shown in Figure A.2. below.

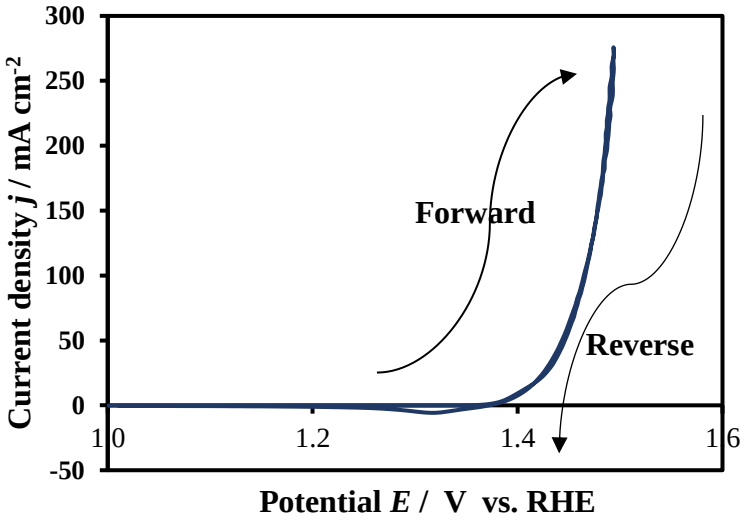


Figure A.2. Typical CV plot with no catalyst oxidation hump. [218]

A hump in the CV curve appears due to catalyst oxidation and reduction. The hump in the forward scan is produced by catalytic metal center oxidizing to produce electron which reflects as an increase in current and the hump in the reverse scan is produced by catalytic metal center reducing back to the oxidation state prior to forward scan. This can be seen in the Figure A.3. shown below.

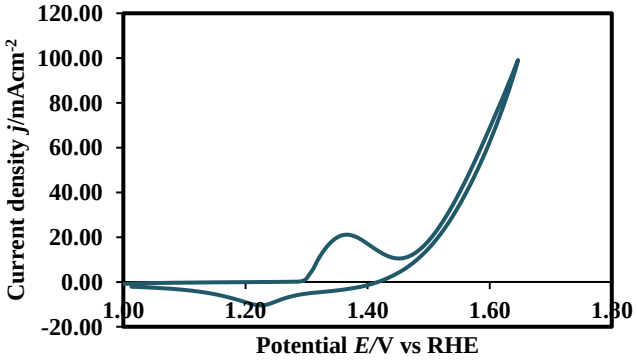


Figure A.3. CV plot showing catalyst oxidation and reduction hump. [Ni doped CeSe, unpublished work from Nath group]

**A.1.3. Chronoamperometry.** It is not just important for the catalyst to perform extremely well for a short period of time. In order to find out, how stable the catalyst is for a prolonged period of time, chronoamperometry is performed. It is done by holding the desired applied potential for several hours to find the change in current response with respect to time. If a degradation in current is observed, it is to be concluded that the catalyst is not stable over a prolonged period of time as can be observed in the blue curve shown in the Figure A.4. Stable performance of the catalyst is depicted by the red curve in the same figure.

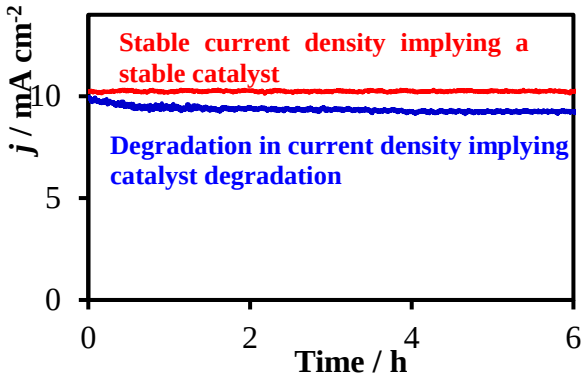


Figure A.4. Typical plot of chronoamperometry of oxygen evolution reaction. [52]

**A.1.4. Kinetics of the Oxygen Evolution Reaction.** In order to understand the kinetics of oxygen evolution reaction, one should understand the Tafel plot and Tafel equation. The fundamental quantities observed in any electrochemical reaction are the current and the potential. The current is a manifestation of the rate of the interfacial reaction and can be shown to be dependent on the applied potential (Bard and Faulkner 2000). The primary concern in electrocatalysis is the relationship between the current and potential. Steady-state Tafel plot analysis is the most widely applied technique in the

study of electrocatalytic reactions. Tafel equation is derived by assuming that there is no mass transport and the reaction takes place purely by kinetic control. Tafel plot is plotted with log of the current density against the corresponding overpotentials. The slope of the Tafel curve is given by the following equation.

$$b = \frac{2.303RT}{n\alpha_a F}$$

Where,

**b** is the slope of the Tafel curve

**R** is the universal gas constant

**T** is the temperature

$\alpha_a$ is the transfer coefficient of the anodic reaction

**F** is the faraday's constant

**n** varies from 1 to 4. n=1 – first electron process, n=2 – second electron process, n=3 – third electron process and n=4 – fourth electron process.

First electron process, n=1 corresponds to that of Eq.=1 in Section 1.3. Second electron process, n=2 corresponds to that of Eq.=2 in Section 1.3. Third electron process, n=3 corresponds to that of Eq.=3 in Section 1.3. Fourth electron process, n=4 corresponds to that of Eq.=4 in Section 1.3.

By solving the equation for the slope by getting the slope from the Tafel curve, value of n can be determined. The value of n obtained gives us which equation is the rate limiting step in the overall OER. This reaction is the slowest step in the overall reaction $4OH^- \rightarrow O_2 + 4H_2O + 4e^-$.

To plot this graph, the points shown in the Figure A.5. below is considered. The region in between the non-faradaic region and region in faradaic region with constant slope is chosen. This region gives the best picture of rate limiting step of the overall OER and this is the region where the reaction takes place due to kinetic control. Beyond this region the reaction takes place due to diffusion control. Classic Tafel plot is shown in the Figure A.6. below.

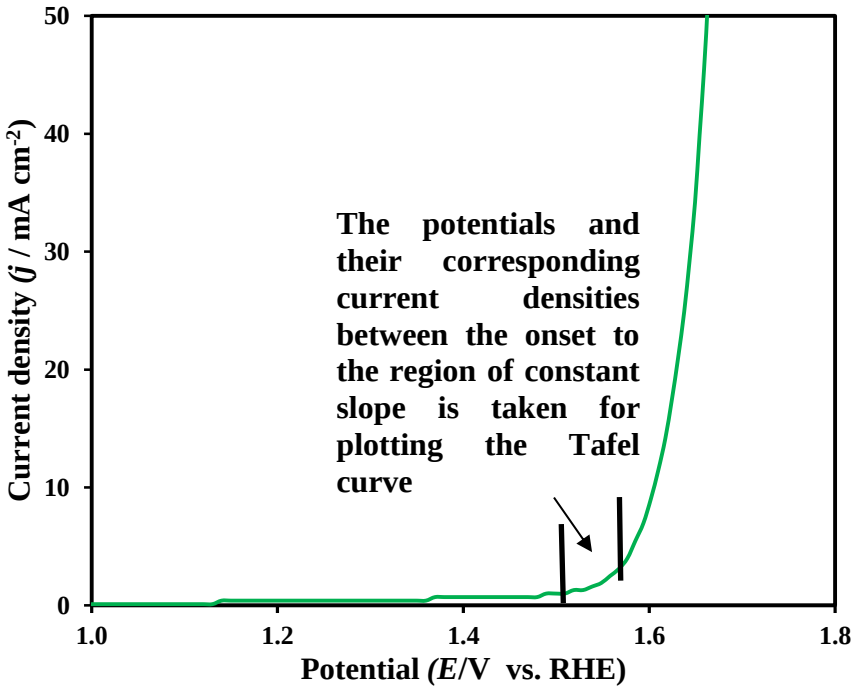


Figure A.5. The region from the LSV curve where the potentials and their corresponding current densities are acquired to plot the Tafel curve. [218]

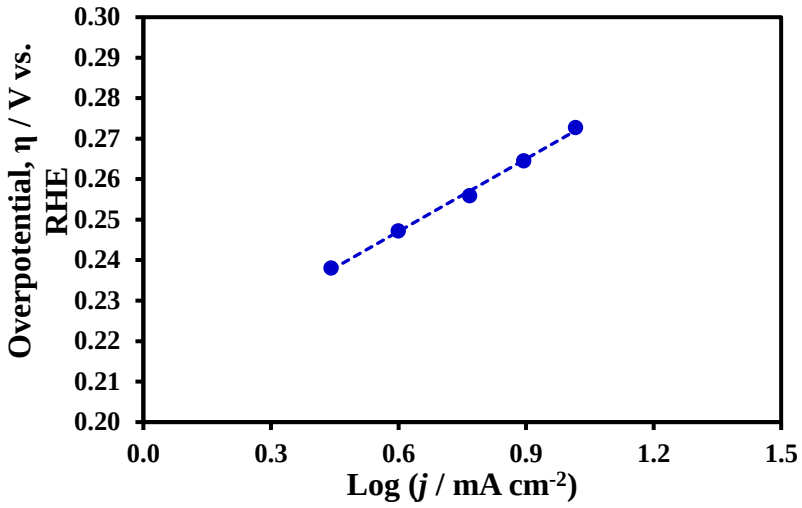


Figure A.6. Typical Tafel plot of oxygen evolution reaction. The slope obtained from this curve is b.[218]

# BIBLIOGRAPHY


[1] DOE Energy Information Administration Transportation (DOE/EIA) internet postings of Annual Energy Outlook, 1995 and International Energy Overview, 1993, and demand statistics through 1993. http://www.eia.doe.gov/oiaf/aeo95/transp_3.cfm. Last visited on 12/13/2017.

[2] Dr. Sarma Pisupati, Products of combustion, EGEE 102 Energy Conservation and Environmental Protection, John A.Dutton e-Education Institute, Penn state college of earth and mineral sciences.

[3] Renewable Energy & Efficiency Partnership (August 2004). "Glossary of terms in sustainable energy regulation" (PDF). Retrieved 2008-12-19.

[4] Jacobson, Mark Z. (2009). "Review of solutions to global warming, air pollution, and energy security". Energy and Environmental Science. Royal Society of Chemistry. 2 (2): 148–173. Retrieved 2008-12-21.

[5] Energy transfers – fuel cells, http://www.bbc.co.uk/schools/gcsebitesize/science/triple_ocr_gateway/chemistry_out_there/energy_transfers/revision/3/, Last accessed on 12/13/2017.

[6] Sapountzi, F.M., Gracia, J.M., Fredriksson, H.O. and Niemantsverdriet, J.H., 2017. Electrocatalysts for the generation of hydrogen, oxygen and synthesis gas. Progress in Energy and Combustion Science, 58, pp.1-35.

[7] Thomas Jaramillo, Energy Tutorial: Electrocatalysis 101, GCEP RESEARCH SYMPOSIUM 2012 | STANFORD, CA.

[8] Bard, A.J., Faulkner, L.R., Leddy, J. and Zoski, C.G., 1980. Electrochemical methods: fundamentals and applications (Vol. 2). New York: wiley.

[9] McCrory, C.C., Jung, S., Ferrer, I.M., Chatman, S.M., Peters, J.C. and Jaramillo, T.F., 2015. Benchmarking hydrogen evolving reaction and oxygen evolving reaction electrocatalysts for solar water splitting devices. J. Am. Chem. Soc, 137(13), pp.4347-4357.

[10] Lewis, N.S. and Nocera, D.G., 2006. Powering the planet: Chemical challenges in solar energy utilization. Proceedings of the National Academy of Sciences, 103(43), pp.15729-15735.

[11] Standard Potentials at 25ºC, http://ch301.cm.utexas.edu/data/standard-potentials.php, Last visited on 12/13/2017.

[12] Krasil'shchikov, A. I., 1963. On the intermediate stages of anodic oxygen evolution Zh. Fiz. Khim., 37, pp.531-537.

[13] Hoare, J. P. The Electrochemistry of Oxygen, Interscience, New York, 1968, pp. 82-91, 284-291.

[14] Bronoel, G. and Reby, J., 1980. Mechanism of oxygen evolution in basic medium at a nickel electrode. Electrochimica Acta, 25(7), pp.973-976.

[15] Bockris, J.O. and Otagawa, T., 1983. Mechanism of oxygen evolution on perovskites. The Journal of Physical Chemistry, 87(15), pp.2960-2971.

[16] Lyons, M.E. and Brandon, M.P., 2008. The oxygen evolution reaction on passive oxide covered transition metal electrodes in aqueous alkaline solution. Part 1-Nickel. Int. J. Electrochem. Sci, 3(12), pp.1386-1424.

[17] Hong, W.T., Risch, M., Stoerzinger, K.A., Grimaud, A., Suntivich, J. and Shao-Horn, Y., 2015. Toward the rational design of non-precious transition metal oxides for oxygen electrocatalysis. Energy & Environmental Science, 8(5), pp.1404-1427.

[18] Trotochaud, L. and Boettcher, S.W., 2014. Precise oxygen evolution catalysts: Status and opportunities. Scripta Materialia, 74, pp.25-32.

[19] Trotochaud, L., Ranney, J.K., Williams, K.N. and Boettcher, S.W., 2012. Solution-cast metal oxide thin film electrocatalysts for oxygen evolution. Journal of the American Chemical Society, 134(41), pp.17253-17261.

[20] Whitesides, G.M. and Crabtree, G.W., 2007. Don't Forget Long-Term Fundamental Research in Energy. Science, 315(5813), pp.796-798.

[21] McCrory, C.C., Jung, S., Peters, J.C. and Jaramillo, T.F., 2013. Benchmarking heterogeneous electrocatalysts for the oxygen evolution reaction. Journal of the American Chemical Society, 135(45), pp.16977-16987.

[22] Fabbri, E., Habereder, A., Waltar, K., Kötz, R. and Schmidt, T.J., 2014. Developments and perspectives of oxide-based catalysts for the oxygen evolution reaction. Catalysis Science & Technology, 4(11), pp.3800-3821.

[23] Suntivich, J., May, K.J., Gasteiger, H.A., Goodenough, J.B. and Shao-Horn, Y., 2011. A perovskite oxide optimized for oxygen evolution catalysis from molecular orbital principles. Science, 334(6061), pp.1383-1385.

[24] Lee, S.W., Carlton, C., Risch, M., Surendranath, Y., Chen, S., Furutsuki, S., Yamada, A., Nocera, D.G. and Shao-Horn, Y., 2012. The nature of lithium battery materials under oxygen evolution reaction conditions. Journal of the American Chemical Society, 134(41), pp.16959-16962.

[25] Mirzakulova, E., Khatmullin, R., Walpita, J., Corrigan, T., Vargas-Barbosa, N.M., Vyas, S., Oottikkal, S., Manzer, S.F., Hadad, C.M. and Glusac, K.D., 2012. Electrode-assisted catalytic water oxidation by a flavin derivative. Nature chemistry, 4(10), pp.794-801.

[26] Rossmeisl, J., Qu, Z.W., Zhu, H., Kroes, G.J. and Nørskov, J.K., 2007. Electrolysis of water on oxide surfaces. Journal of Electroanalytical Chemistry, 607(1), pp.83-89.

[27] Lee, Y., Suntivich, J., May, K.J., Perry, E.E. and Shao-Horn, Y., 2012. Synthesis and activities of rutile $IrO_2$ and $RuO_2$ nanoparticles for oxygen evolution in acid and alkaline solutions. The journal of physical chemistry letters, 3(3), pp.399-404.

[28] Gong, M. and Dai, H., 2015. A mini review of NiFe-based materials as highly active oxygen evolution reaction electrocatalysts. Nano Research, 8(1), pp.23-39.

[29] Wang, H.Y., Hsu, Y.Y., Chen, R., Chan, T.S., Chen, H.M. and Liu, B., 2015. $Ni^{3+}$-Induced Formation of Active NiOOH on the Spinel Ni–Co Oxide Surface for Efficient Oxygen Evolution Reaction. Advanced Energy Materials, 5(10).

[30] Gardner, G.P., Go, Y.B., Robinson, D.M., Smith, P.F., Hadermann, J., Abakumov, A., Greenblatt, M. and Dismukes, G.C., 2012. Structural requirements in lithium cobalt oxides for the catalytic oxidation of water. Angewandte Chemie International Edition, 51(7), pp.1616-1619.

[31] Li, Y., Hasin, P. and Wu, Y., 2010. $Ni_xCo_{3-x}O_4$ nanowire arrays for electrocatalytic oxygen evolution. Advanced materials, 22(17), pp.1926-1929.

[32] Landon, J., Demeter, E., İnoğlu, N., Keturakis, C., Wachs, I.E., Vasić, R., Frenkel, A.I. and Kitchin, J.R., 2012. Spectroscopic characterization of mixed Fe–Ni oxide electrocatalysts for the oxygen evolution reaction in alkaline electrolytes. ACS Catalysis, 2(8), pp.1793-1801.

[33] Gong, M., Li, Y., Wang, H., Liang, Y., Wu, J.Z., Zhou, J., Wang, J., Regier, T., Wei, F. and Dai, H., 2013. An advanced Ni–Fe layered double hydroxide electrocatalyst for water oxidation. J. Am. Chem. Soc, 135(23), pp.8452-8455.

[34] Chen, S. and Qiao, S.Z., 2013. Hierarchically porous nitrogen-doped graphene–$NiCo_2O_4$ hybrid paper as an advanced electrocatalytic water-splitting material. ACS Nano, *7*(11), pp.10190-10196.

[35] Chen, S., Duan, J., Jaroniec, M. and Qiao, S.Z., 2013. Three-dimensional N-doped graphene hydrogel/NiCo double hydroxide electrocatalysts for highly efficient oxygen evolution. Angewandte Chemie International Edition, 52(51), pp.13567-13570.

[36] Gao, M.R., Xu, Y.F., Jiang, J., Zheng, Y.R. and Yu, S.H., 2012. Water oxidation electrocatalyzed by an efficient $Mn_3O_4/CoSe_2$ nanocomposite. Journal of the American Chemical Society, 134(6), pp.2930-2933.

[37] Gao, M., Sheng, W., Zhuang, Z., Fang, Q., Gu, S., Jiang, J. and Yan, Y., 2014. Efficient water oxidation using nanostructured α-nickel-hydroxide as an electrocatalyst. Journal of the American Chemical Society, 136(19), pp.7077-7084.

[38] Zhao, Z., Wu, H., He, H., Xu, X. and Jin, Y., 2015. Self-standing non-noble metal (Ni–Fe) oxide nanotube array anode catalysts with synergistic reactivity for high-performance water oxidation. Journal of Materials Chemistry A, 3(13), pp.7179-7186.

[39] Zhao, Z., Wu, H., He, H., Xu, X. and Jin, Y., 2014. A High-Performance Binary Ni–Co Hydroxide-based Water Oxidation Electrode with Three-Dimensional Coaxial Nanotube Array Structure. Advanced Functional Materials, 24(29), pp.4698-4705.

[40] Jiang, J., Zhang, A., Li, L. and Ai, L., 2015. Nickel–cobalt layered double hydroxide nanosheets as high-performance electrocatalyst for oxygen evolution reaction. Journal of Power Sources, 278, pp.445-451.

[41] Gao, M.R., Xu, Y.F., Jiang, J. and Yu, S.H., 2013. Nanostructured metal chalcogenides: synthesis, modification, and applications in energy conversion and storage devices. Chemical Society Reviews, 42(7), pp.2986-3017.

[42] Hong, W.T., Risch, M., Stoerzinger, K.A., Grimaud, A., Suntivich, J. and Shao-Horn, Y., 2015. Toward the rational design of non-precious transition metal oxides for oxygen electrocatalysis. Energy & Environmental Science, 8(5), pp.1404-1427.

[43] Rosalbino, F., Delsante, S., Borzone, G. and Scavino, G., 2013. Electrocatalytic activity of crystalline Ni–Co–M (M= Cr, Mn, Cu) alloys on the oxygen evolution reaction in an alkaline environment. International Journal of Hydrogen Energy, 38(25), pp.10170-10177.

[44] Hammer, B. and Nørskov, J.K., 2000. Theoretical surface science and catalysis—calculations and concepts. Advances in catalysis, 45, pp.71-129.

[45] Nørskov, J.K., Bligaard, T., Rossmeisl, J. and Christensen, C.H., 2009. Towards the computational design of solid catalysts. Nature chemistry, 1(1), pp.37-46.

[46] Surendranath, Y., Kanan, M.W. and Nocera, D.G., 2010. Mechanistic studies of the oxygen evolution reaction by a cobalt-phosphate catalyst at neutral pH. Journal of the American Chemical Society, 132(46), pp.16501-16509.

[47] Sun, Y., Bigi, J.P., Piro, N.A., Tang, M.L., Long, J.R. and Chang, C.J., 2011. Molecular cobalt pentapyridine catalysts for generating hydrogen from water. Journal of the American Chemical Society, 133(24), pp.9212-9215.

[48] Kärkäs, M.D., Verho, O., Johnston, E.V. and Åkermark, B., 2014. Artificial photosynthesis: molecular systems for catalytic water oxidation. Chemical reviews, 114(24), pp.11863-12001.

[49] Faunce, T., Styring, S., Wasielewski, M.R., Brudvig, G.W., Rutherford, A.W., Messinger, J., Lee, A.F., Hill, C.L., Fontecave, M., MacFarlane, D.R. and Hankamer, B., 2013. Artificial photosynthesis as a frontier technology for energy sustainability. Energy & Environmental Science, 6(4), pp.1074-1076.

[50] Nocera, D.G., 2012. The artificial leaf. Accounts of Chemical Research, 45(5), pp.767-776.

[51] Swesi, A.T., Masud, J. and Nath, M., 2016. Nickel selenide as a high-efficiency catalyst for oxygen evolution reaction. Energy & Environmental Science, 9(5), pp.1771-1782.

[52] Swesi, A.T., Masud, J. and Nath, M., 2016. Enhancing electrocatalytic activity of bifunctional $Ni_3Se_2$ for overall water splitting through etching-induced surface nanostructuring. Journal of Materials Research, 31(18), pp.2888-2896.

[53] Swesi, A.T., Masud, J., Liyanage, W.P., Umapathi, S., Bohannan, E., Medvedeva, J. and Nath, M., 2017. Textured NiSe 2 Film: Bifunctional Electrocatalyst for Full Water Splitting at Remarkably Low Overpotential with High Energy Efficiency. Scientific Reports, 7(1), p.2401.

[54] Masud, J., Swesi, A.T., Liyanage, W.P. and Nath, M., 2016. Cobalt selenide nanostructures: an efficient bifunctional catalyst with high current density at low coverage. ACS applied materials & interfaces, 8(27), pp.17292-17302.

[55] Swesi, A. T.; Masud, J.; Nath, M. New Family of High-Efficiency Oxygen Evolution Electrocatalyst Based on Ni-Fe Mixed Chalcogenides. Paper #3335, PRiME 2016, ECS Meeting. Masud, J.; Liyanage, W. P. R.; Nath, M. A Simple Non-expensive Binary Metal Selenide for Electrocatalytic Water Oxidation with High Efficiency at Low Overpotentials (submitted to Scientific Reports). Golrokhamen, B.; Swesi, A. T.; Masud, J.; Nath, M., 2017. Cobalt nickel selenide as an efficienct bifunctional electrocatalyst for overall water splitting Chemical Communication 53, pp.5412-5415. De Silva, U.; Masud, J.; Nath, M. Nickel Telluride as Highly Efficient Water Oxidation Electrocatalyst; Cao, X.; Masud, J.; Nath, M. Combinatorial Approach towards discovery of mixed metal selenide OER electrocatalysts (submitted to Energy and Environmental Science).

[56] Inorganic Chemistry ($5^{th}$ edition) Gary Meissler, Paul Fischer, Donald A. Tarr 2014, Prentice Hall.

[57] Masud, J., Ioannou, P.C., Levesanos, N., Kyritsis, P. and Nath, M., 2016. A Molecular Ni-complex Containing Tetrahedral Nickel Selenide Core as Highly Efficient Electrocatalyst for Water Oxidation. ChemSusChem, 9(22), pp.3128-3132.

[58] Shein, I.R., Medvedeva, N.I. and Ivanovskii, A.L., 2006. Electronic and structural properties of cementite-type $M_3X$ (M= Fe, Co, Ni; X= C or B) by first principles calculations. Physica B: Condensed Matter, 371(1), pp.126-132.

[59] Gumeniuk, R., Borrmann, H. and Leithe-Jasper, A., 2006. Refinement of the crystal structures of trinickel boron, $Ni_3B$, and tripalladium boron, $Pd_3B$. Zeitschrift für Kristallographie-New Crystal Structures, 221(1-4), pp.425-426.

[60] Wyckoff, R.W.G. (1964) Crystal Structures, Vol. 2. 2nd Edition, John Wiley & Sons, Inc., New York, London, Sydney.

[61] Carenco, S., Portehault, D., Boissiere, C., Mezailles, N. and Sanchez, C., 2013. Nanoscaled metal borides and phosphides: recent developments and perspectives. Chemical reviews, 113(10), pp.7981-8065.

[62] Finch, C.B., Ferber, M.K., Simpson, W.A. and Williams, R.K., 1984. Anisotropy of thermal expansion, elasticity, and electrical resistivity in single-crystal trinickel boride, $Ni_3B$. Journal of materials science letters, 3(12), pp.1074-1076.

[63] Kul'ba, Y.K. and Vinitskii, I.M., 1992. Structure evolution and electrical conductivity of thick films based on dispersed $Ni_3B$ powders. Soviet powder metallurgy and metal ceramics, 31(3), pp.251-255.

[64] Fahrenholtz, W.G., Wuchina, E.J., Lee, W.E. and Zhou, Y. eds., 2014. Ultra-high temperature ceramics: materials for extreme environment applications. John Wiley & Sons.

[65] Schaefer, Z.L., Ke, X., Schiffer, P. and Schaak, R.E., 2008. Direct solution synthesis, reaction pathway studies, and structural characterization of crystalline $Ni_3B$ nanoparticles. The Journal of Physical Chemistry C, 112(50), pp.19846-19851.

[66] Felix, C., Maiyalagan, T., Pasupathi, S., Bladergroen, B. and Linkov, V., 2012. Synthesis and optimisation of $IrO_2$ electrocatalysts by Adams fusion method for solid polymer electrolyte electrolysers. Micro and nanosystems, 4(3), pp.186-191.

[67] Zhao, Y., Hernandez-Pagan, E.A., Vargas-Barbosa, N.M., Dysart, J.L. and Mallouk, T.E., 2011. A high yield synthesis of ligand-free iridium oxide nanoparticles with high electrocatalytic activity. The Journal of Physical Chemistry Letters, 2(5), pp.402-406.

[68] Nakagawa, T., Bjorge, N.S. and Murray, R.W., 2009. Electrogenerated $IrO_x$ nanoparticles as dissolved redox catalysts for water oxidation. Journal of the American Chemical Society, 131(43), pp.15578-15579.

[69] Nakagawa, T., Beasley, C.A. and Murray, R.W., 2009. Efficient electro-oxidation of water near its reversible potential by a mesoporous $IrO_x$ nanoparticle film. The Journal of Physical Chemistry C, 113(30), pp.12958-12961.

[70] Abbott, D.F., Lebedev, D., Waltar, K., Povia, M., Nachtegaal, M., Fabbri, E., Copéret, C. and Schmidt, T.J., 2016. Iridium oxide for the oxygen evolution reaction: correlation between particle size, morphology, and the surface hydroxo layer from operando XAS. Chemistry of Materials, 28(18), pp.6591-6604.

[71] Wang, D., Chen, X., Evans, D.G. and Yang, W., 2013. Well-dispersed $Co_3O_4/Co_2MnO_4$ nanocomposites as a synergistic bifunctional catalyst for oxygen reduction and oxygen evolution reactions. Nanoscale, 5(12), pp.5312-5315.

[72] Song, W., Ren, Z., Chen, S.Y., Meng, Y., Biswas, S., Nandi, P., Elsen, H.A., Gao, P.X. and Suib, S.L., 2016. Ni-and Mn-promoted mesoporous $Co_3O_4$: a stable bifunctional catalyst with surface-structure-dependent activity for oxygen reduction reaction and oxygen evolution reaction. ACS applied materials & interfaces, 8(32), pp.20802-20813.

[73] Jiao, F. and Frei, H., 2009. Nanostructured Cobalt Oxide Clusters in Mesoporous Silica as Efficient Oxygen-Evolving Catalysts. Angewandte Chemie International Edition, 48(10), pp.1841-1844.

[74] Lutterman, D.A., Surendranath, Y. and Nocera, D.G., 2009. A self-healing oxygen-evolving catalyst. Journal of the American Chemical Society, 131(11), pp.3838-3839.

[75] Bajdich, M., García-Mota, M., Vojvodic, A., Nørskov, J.K. and Bell, A.T., 2013. Theoretical investigation of the activity of cobalt oxides for the electrochemical oxidation of water. Journal of the American chemical Society, 135(36), pp.13521-13530.

[76] García-Mota, M., Bajdich, M., Viswanathan, V., Vojvodic, A., Bell, A.T. and Nørskov, J.K., 2012. Importance of correlation in determining electrocatalytic oxygen evolution activity on cobalt oxides. The Journal of Physical Chemistry C, 116(39), pp.21077-21082.

[77] Li, Z., Yu, X.Y. and Paik, U., 2016. Facile preparation of porous $Co_3O_4$ nanosheets for high-performance lithium ion batteries and oxygen evolution reaction. Journal of Power Sources, 310, pp.41-46.

[78] Yao, L., Zhong, H., Deng, C., Li, X. and Zhang, H., 2016. Template-assisted synthesis of hierarchically porous $Co_3O_4$ with enhanced oxygen evolution activity. Journal of Energy Chemistry, 25(1), pp.153-157.

[79] Yang, X., Li, H., Lu, A.Y., Min, S., Idriss, Z., Hedhili, M.N., Huang, K.W., Idriss, H. and Li, L.J., 2016. Highly acid-durable carbon coated $Co_3O_4$ nanoarrays as efficient oxygen evolution electrocatalysts. Nano Energy, 25, pp.42-50.

[80] Liu, Y.R., Han, G.Q., Li, X., Dong, B., Shang, X., Hu, W.H., Chai, Y.M., Liu, Y.Q. and Liu, C.G., 2016. A facile synthesis of reduced $Co_3O_4$ nanoparticles with enhanced Electrocatalytic activity for oxygen evolution. International Journal of Hydrogen Energy, 41(30), pp.12976-12982.

[81] Wu, Z., Sun, L.P., Yang, M., Huo, L.H., Zhao, H. and Grenier, J.C., 2016. Facile synthesis and excellent electrochemical performance of reduced graphene oxide–$Co_3O_4$ yolk-shell nanocages as a catalyst for oxygen evolution reaction. Journal of Materials Chemistry A, 4(35), pp.13534-13542.

[82] Balakrishnan, T., Anis, M., Arun, S., Kumar, M. and Mayavan, S., 2016. BCN–$Co_3O_4$ hybrid–a highly efficient catalyst for the oxygen evolution reaction and dye degradation. RSC Advances, 6(83), pp.79448-79451.

[83] Zhang, L., Li, H., Li, K., Li, L., Wei, J., Feng, L. and Fu, Q., 2016. Morphology-controlled fabrication of $Co_3O_4$ nanostructures and their comparative catalytic activity for oxygen evolution reaction. Journal of Alloys and Compounds, 680, pp.146-154.

[84] Zhang, C., Xiao, J., Lv, X., Qian, L., Yuan, S., Wang, S. and Lei, P., 2016. Hierarchically porous $Co_3O_4$/C nanowire arrays derived from a metal–organic framework for high performance supercapacitors and the oxygen evolution reaction. Journal of Materials Chemistry A, 4(42), pp.16516-16523.

[85] Dou, Y., Liao, T., Ma, Z., Tian, D., Liu, Q., Xiao, F., Sun, Z., Kim, J.H. and Dou, S.X., 2016. Graphene-like holey $Co_3O_4$ nanosheets as a highly efficient catalyst for oxygen evolution reaction. Nano Energy, 30, pp.267-275.

[86] Fang, Y., Li, X., Hu, Y., Li, F., Lin, X., Tian, M., An, X., Fu, Y., Jin, J. and Ma, J., 2015. Ultrasonication-assisted ultrafast preparation of multiwalled carbon nanotubes/Au/$Co_3O_4$ tubular hybrids as superior anode materials for oxygen evolution reaction. Journal of Power Sources, 300, pp.285-293.

[87] Ramsundar, R.M., Debgupta, J., Pillai, V.K. and Joy, P.A., 2015. $Co_3O_4$ Nanorods—Efficient Non-noble Metal Electrocatalyst for Oxygen Evolution at Neutral pH. Electrocatalysis, 6(4), pp.331-340.

[88] Bergmann, A., Martinez-Moreno, E., Teschner, D., Chernev, P., Gliech, M., De Araújo, J.F., Reier, T., Dau, H. and Strasser, P., 2015. Reversible amorphization and the catalytically active state of crystalline $Co_3O_4$ during oxygen evolution. Nature communications, 6.

[89] Zhang, Y., Ding, F., Deng, C., Zhen, S., Li, X., Xue, Y., Yan, Y.M. and Sun, K., 2015. Crystal plane-dependent electrocatalytic activity of $Co_3O_4$ toward oxygen evolution reaction. Catalysis Communications, 67, pp.78-82.

[90] Zhang, P., Dong, Y., Kou, Y., Yang, Z., Li, Y. and Sun, X., 2015. First-Principles Study of Oxygen Evolution Reaction on the Oxygen-Containing Species Covered CoII-Exposing $Co_3O_4$ (100) Surface. Catalysis Letters, 145(5), pp.1169-1176.

[91] Zhao, Y., Chen, S., Sun, B., Su, D., Huang, X., Liu, H., Yan, Y., Sun, K. and Wang, G., 2015. Graphene-$Co_3O_4$ nanocomposite as electrocatalyst with high performance for oxygen evolution reaction. Scientific reports, 5, p.7629.

[92] Wu, L.K. and Hu, J.M., 2014. A silica co-electrodeposition route to nanoporous $Co_3O_4$ film electrode for oxygen evolution reaction. Electrochimica Acta, 116, pp.158-163.

[93] Liu, Y.C., Koza, J.A. and Switzer, J.A., 2014. Conversion of electrodeposited Co $(OH)_2$ to CoOOH and $Co_3O_4$, and comparison of their catalytic activity for the oxygen evolution reaction. Electrochimica Acta, 140, pp.359-365.

[94] Wu, X. and Scott, K., 2013. A Li-doped $Co_3O_4$ oxygen evolution catalyst for non-precious metal alkaline anion exchange membrane water electrolysers. International Journal of Hydrogen Energy, 38(8), pp.3123-3129.

[95] Suryanto, B.H., Lu, X. and Zhao, C., 2013. Layer-by-layer assembly of transparent amorphous $Co_3O_4$ nanoparticles/graphene composite electrodes for sustained oxygen evolution reaction. Journal of Materials Chemistry A, 1(41), pp.12726-12731.

[96] Fan, Y., Zhang, N., Zhang, L., Shao, H., Wang, J., Zhang, J. and Cao, C., 2013. Synthesis of small-sized freestanding $Co_3O_4$ nanosheets with improved activity for $H_2O_2$ sensing and oxygen evolution. Journal of The Electrochemical Society, 160(2), pp.F218-F223.

[97] Zou, X., Su, J., Silva, R., Goswami, A., Sathe, B.R. and Asefa, T., 2013. Efficient oxygen evolution reaction catalyzed by low-density Ni-doped $Co_3O_4$ nanomaterials derived from metal-embedded graphitic $C_3N_4$. Chemical Communications, 49(68), pp.7522-7524.

[98] Zhang, N., Fan, Y., Fan, H., Shao, H., Wang, J., Zhang, J. and Cao, C., 2012. Cross-linked $Co_3O_4$ nanowalls synthesized by electrochemical oxidation of metallic cobalt layer for oxygen evolution. ECS Electrochemistry Letters, 1(2), pp.H8-H10.

[99] Lu, B., Cao, D., Wang, P., Wang, G. and Gao, Y., 2011. Oxygen evolution reaction on Ni-substituted $Co_3O_4$ nanowire array electrodes. International Journal of Hydrogen Energy, 36(1), pp.72-78.

[100] Palmas, S., Ferrara, F., Mascia, M., Polcaro, A.M., Ruiz, J.R., Vacca, A. and Piccaluga, G., 2009. Modeling of oxygen evolution at Teflon-bonded Ti/$Co_3O_4$ electrodes. International Journal of Hydrogen Energy, 34(4), pp.1647-1654.

[101] Singh, N.K., Singh, J.P. and Singh, R.N., 2002. Sol–gel-derived spinel $Co_3O_4$ films and oxygen evolution: Part II. Optimization of preparation conditions and influence of the nature of the metal salt precursor. International journal of hydrogen energy, 27(9), pp.895-903.

[102] Wang, Q., Qiu, X., Hu, W. and Huang, Y., 2017. Facile synthesis of three-dimensional porous nitrogen doped carbon supported $Co_3O_4$ for oxygen reduction reaction and oxygen evolution reaction. Materials Letters, 190, pp.169-172.

[103] Yu, D., Xu, C., Su, Y., Liu, D. and He, X., 2017. Nitrogen-doped graphene aerogels-supported cobaltosic oxide nanocrystals as high-performance bi-functional electrocatalysts for oxygen reduction and evolution reactions. Journal of Electroanalytical Chemistry, 787, pp.46-54.

[104] Plaisance, C.P., Reuter, K. and van Santen, R.A., 2016. Quantum chemistry of the oxygen evolution reaction on cobalt (II, III) oxide–implications for designing the optimal catalyst. Faraday discussions, 188, pp.199-226.

[105] Jiang, N., Bogoev, L., Popova, M., Gul, S., Yano, J. and Sun, Y., 2014. Electrodeposited nickel-sulfide films as competent hydrogen evolution catalysts in neutral water. Journal of Materials Chemistry A, 2(45), pp.19407-19414.

[106] Chung, D.Y., Han, J.W., Lim, D.H., Jo, J.H., Yoo, S.J., Lee, H. and Sung, Y.E., 2015. Structure dependent active sites of $Ni_xS_y$ as electrocatalysts for hydrogen evolution reaction. Nanoscale, 7(12), pp.5157-5163.

[107] Zhou, W., Wu, X.J., Cao, X., Huang, X., Tan, C., Tian, J., Liu, H., Wang, J. and Zhang, H., 2013. $Ni_3S_2$ nanorods/Ni foam composite electrode with low overpotential for electrocatalytic oxygen evolution. Energy & Environmental Science, 6(10), pp.2921-2924.

[108] Feng, L.L., Yu, G., Wu, Y., Li, G.D., Li, H., Sun, Y., Asefa, T., Chen, W. and Zou, X., 2015. High-index faceted $Ni_3S_2$ nanosheet arrays as highly active and ultrastable electrocatalysts for water splitting. J. Am. Chem. Soc, 137(44), pp.14023-14026.

[109] Feng, Y., He, T. and Alonso-Vante, N., 2007. In situ free-surfactant synthesis and ORR-electrochemistry of carbon-supported $Co_3S_4$ and $CoSe_2$ nanoparticles. Chemistry of Materials, 20(1), pp.26-28.

[110] Li, R., Dai, Y., Chen, B., Zou, J., Jiang, B. and Fu, H., 2016. Nitrogen-doped Co/$Co_9S_8$/partly-graphitized carbon as durable catalysts for oxygen reduction in microbial fuel cells. Journal of Power Sources, 307, pp.1-10.

[111] Wang, H., Liang, Y., Li, Y. and Dai, H., 2011. Co1−xS–Graphene Hybrid: A High-Performance Metal Chalcogenide Electrocatalyst for Oxygen Reduction. Angewandte Chemie International Edition, 50(46), pp.10969-10972.

[112] Falkowski, J.M. and Surendranath, Y., 2015. Metal chalcogenide nanofilms: platforms for mechanistic studies of electrocatalysis. ACS Catalysis, 5(6), pp.3411-3416.

[113] Zhong, H., Li, K., Zhang, Q., Wang, J., Meng, F., Wu, Z., Yan, J. and Zhang, X., 2016. In situ anchoring of $Co_9S_8$ Nanoparticles on N and S Co-Doped porous carbon tube as bifunctional oxygen electrocatalysts, NPG Asia Mater 8 (2016) e308.

[114] Liu, Q. and Zhang, J., 2013. A general and controllable synthesis of $Co_mS_n$ ($Co_9S_8$, $Co_3S_4$, and Co 1−x S) hierarchical microspheres with homogeneous phases. CrystEngComm, 15(25), pp.5087-5092.

[115] Wang, J., Zhong, H.X., Wang, Z.L., Meng, F.L. and Zhang, X.B., 2016. Integrated three-dimensional carbon paper/carbon tubes/cobalt-sulfide sheets as an efficient electrode for overall water splitting.

[116] Yang, J., Zhu, G., Liu, Y., Xia, J., Ji, Z., Shen, X. and Wu, S., 2016. $Fe_3O_4$-Decorated $Co_9S_8$ Nanoparticles In Situ Grown on Reduced Graphene Oxide: A New and Efficient Electrocatalyst for Oxygen Evolution Reaction. Advanced Functional Materials, 26(26), pp.4712-4721.

[117] Liu, T., Liang, Y., Liu, Q., Sun, X., He, Y. and Asiri, A.M., 2015. Electrodeposition of cobalt-sulfide nanosheets film as an efficient electrocatalyst for oxygen evolution reaction. Electrochemistry Communications, 60, pp.92-96.

[118] Liu, Y., Cheng, H., Lyu, M., Fan, S., Liu, Q., Zhang, W., Zhi, Y., Wang, C., Xiao, C., Wei, S. and Ye, B., 2014. Low overpotential in vacancy-rich ultrathin $CoSe_2$ nanosheets for water oxidation. Journal of the American Chemical Society, 136(44), pp.15670-15675.

[119] Yu, X.Y., Feng, Y., Guan, B., Lou, X.W.D. and Paik, U., 2016. Carbon coated porous nickel phosphides nanoplates for highly efficient oxygen evolution reaction. Energy & Environmental Science, 9(4), pp.1246-1250.

[120] Kher, S.S. and Spencer, J.T., 1992. Chemical vapor deposition precursor chemistry. 3. Formation and characterization of crystalline nickel boride thin films from the cluster-assisted deposition of polyhedral borane compounds. Chemistry of materials, 4(3), pp.538-544.

[121] Bonny, A., Brewster, R. and Welborn, A., 1982. Novel metal borides with catalyitc reactivity for hydrodesulfurization and coal liquefaction. Inorganica Chimica Acta, 64, pp.L3-L5.

[122] Bonny, A.M., 1984. Polyborane-derived metal borides. 1. Hydrodesulphurization catalysts with potential for coal liquefaction. Fuel, 63(10), pp.1410-1413.

[123] Skrabalak, S.E. and Suslick, K.S., 2006. On the possibility of metal borides for hydrodesulfurization. Chemistry of materials, 18(13), pp.3103-3107.

[124] Parks, G.L., Pease, M.L., Burns, A.W., Layman, K.A., Bussell, M.E., Wang, X., Hanson, J. and Rodriguez, J.A., 2007. Characterization and hydrodesulfurization properties of catalysts derived from amorphous metal-boron materials. Journal of Catalysis, 246(2), pp.277-292.

[125] Qi, X.; Shi, Q.; Chen, W.; Zhang, R. Chin. J. Catal. 2012, 33, 543.

[126] Stewart, A. C.; Schaeffer, G. W. J. Inorg. Nucl. Chem. 1956, 3, 194.

[127] Schaeffer, G.W., Roscoe, J.S. and Stewart, A.C., 1956. The Reduction of Iron (III) Chloride with Lithium Aluminohydride and Lithium Borohydride: Iron (II) Borohydride1. Journal of the American Chemical Society, 78(4), pp.729-733.

[128] Brown, H.C. and Brown, C.A., 1963. The Reaction of Sodium Borohydride with Nickel Acetate in Ethanol Solution--A Highly Selective Nickel Hydrogenation Catalyst. Journal of the American Chemical Society, 85(7), pp.1005-1006.

[129] Maybury, P. C.; Mitchell, R. W.; Hawthorne, M. F. J. Chem. Soc., Chem. Commun. 1974, 534.

[130] Schaefer, Z.L., Ke, X., Schiffer, P. and Schaak, R.E., 2008. Direct solution synthesis, reaction pathway studies, and structural characterization of crystalline $Ni_3B$ nanoparticles. The Journal of Physical Chemistry C, 112(50), pp.19846-19851.

[131] Schlesinger, H.; Brown, H. C.; Finholt, A.; Gilbreath, J. R.; Hoekstra, H. R.; Hyde, E. K. J. Am. Chem. Soc. 1953, 75, 215.

[132] Glavee, G.N., Klabunde, K.J., Sorensen, C.M. and Hadjapanayis, G.C., 1992. Borohydride reductions of metal ions. A new understanding of the chemistry leading to nanoscale particles of metals, borides, and metal borates. Langmuir, 8(3), pp.771-773.

[133] Glavee, G.N., Klabunde, K.J., Sorensen, C.M. and Hadjipanayis, G.C., 1993. Borohydride reduction of cobalt ions in water. Chemistry leading to nanoscale metal, boride, or borate particles. Langmuir, 9(1), pp.162-169.

[134] Levy, A., Brown, J.B. and Lyons, C.J., 1960. Catalyzed hydrolysis of sodium borohydride. Industrial & Engineering Chemistry, 52(3), pp.211-214.

[135] Tian, G.L., Zhao, M.Q., Yu, D., Kong, X.Y., Huang, J.Q., Zhang, Q. and Wei, F., 2014. Nitrogen-Doped Graphene/Carbon Nanotube Hybrids: In Situ Formation on Bifunctional Catalysts and Their Superior Electrocatalytic Activity for Oxygen Evolution/Reduction Reaction. Small, 10(11), pp.2251-2259.

[136] Zhang, J., Zhao, Z., Xia, Z. and Dai, L., 2015. A metal-free bifunctional electrocatalyst for oxygen reduction and oxygen evolution reactions. Nature nanotechnology, 10(5), pp.444-452.

[137] Chen, S., Duan, J., Jaroniec, M. and Qiao, S.Z., 2014. Nitrogen and Oxygen Dual-Doped Carbon Hydrogel Film as a Substrate-Free Electrode for Highly Efficient Oxygen Evolution Reaction. Advanced Materials, 26(18), pp.2925-2930.

[138] Zhao, Y., Nakamura, R., Kamiya, K., Nakanishi, S. and Hashimoto, K., 2013. Nitrogen-doped carbon nanomaterials as non-metal electrocatalysts for water oxidation. Nature communications, 4, p.2390.

[139] Lu, X., Yim, W.L., Suryanto, B.H. and Zhao, C., 2015. Electrocatalytic oxygen evolution at surface-oxidized multiwall carbon nanotubes. Journal of the American Chemical Society, 137(8), pp.2901-2907.

[140] Cheng, Y., Xu, C., Jia, L., Gale, J.D., Zhang, L., Liu, C., Shen, P.K. and Jiang, S.P., 2015. Pristine carbon nanotubes as non-metal electrocatalysts for oxygen evolution reaction of water splitting. Applied Catalysis B: Environmental, 163, pp.96-104.

[141] Zhao, J., Liu, Y., Quan, X., Chen, S., Zhao, H. and Yu, H., 2016. Nitrogen and sulfur co-doped graphene/carbon nanotube as metal-free electrocatalyst for oxygen evolution reaction: the enhanced performance by sulfur doping. Electrochimica Acta, 204, pp.169-175.

[142] Balogun, M.S., Qiu, W., Yang, H., Fan, W., Huang, Y., Fang, P., Li, G., Ji, H. and Tong, Y., 2016. A monolithic metal-free electrocatalyst for oxygen evolution reaction and overall water splitting. Energy & Environmental Science, 9(11), pp.3411-3416.

[143] Xiao, Z., Huang, X., Xu, L., Yan, D., Huo, J. and Wang, S., 2016. Edge-selectively phosphorus-doped few-layer graphene as an efficient metal-free electrocatalyst for the oxygen evolution reaction. Chemical Communications, 52(88), pp.13008-13011.

[144] Cheng, N., Liu, Q., Tian, J., Xue, Y., Asiri, A.M., Jiang, H., He, Y. and Sun, X., 2015. Acidically oxidized carbon cloth: a novel metal-free oxygen evolution electrode with high catalytic activity. Chemical Communications, 51(9), pp.1616-1619.

[145] Chao, S. and Geng, M., 2016. 3, 5-Diamino-1, 2, 4-triazole as a Nitrogen precursor to synthesize highly efficient Co-N/C non-precious metal bifunctional catalyst for oxygen reduction reaction and oxygen evolution reaction. International Journal of Hydrogen Energy, 41(30), pp.12995-13004.

[146] Wang, J., Li, K., Zhong, H.X., Xu, D., Wang, Z.L., Jiang, Z., Wu, Z.J. and Zhang, X.B., 2015. Synergistic Effect between Metal–Nitrogen–Carbon Sheets and NiO Nanoparticles for Enhanced Electrochemical Water-Oxidation Performance. Angewandte Chemie International Edition, 54(36), pp.10530-10534.

[147] Wang, H.F., Tang, C. and Zhang, Q., 2015. Towards superior oxygen evolution through graphene barriers between metal substrates and hydroxide catalysts. Journal of Materials Chemistry A, 3(31), pp.16183-16189.

[148] Abdelhafiz, A., Vitale, A., Joiner, C., Vogel, E. and Alamgir, F.M., 2015. Layer-by-layer evolution of structure, strain, and activity for the oxygen evolution reaction in graphene-templated Pt monolayers. ACS applied materials & interfaces, 7(11), pp.6180-6188.

[149] Lu, X., Chan, H.M., Sun, C.L., Tseng, C.M. and Zhao, C., 2015. Interconnected core–shell carbon nanotube–graphene nanoribbon scaffolds for anchoring cobalt oxides as bifunctional electrocatalysts for oxygen evolution and reduction. Journal of Materials Chemistry A, 3(25), pp.13371-13376.

[150] Zhao, M., Li, X., Song, L., He, D. and Zhang, Z., 2016. Substrate-Assisted Deposition of Metal Oxides on Three-Dimensional Porous Reduced Graphene Oxide Networks as Bifunctional Hybrid Electrocatalysts for the Oxygen Evolution and Oxygen Reduction Reactions. ChemCatChem, 8(17), pp.2808-2816.

[151] Sun, J., Yin, H., Liu, P., Wang, Y., Yao, X., Tang, Z. and Zhao, H., 2016. Molecular engineering of Ni–/Co–porphyrin multilayers on reduced graphene oxide sheets as bifunctional catalysts for oxygen evolution and oxygen reduction reactions. Chemical Science, 7(9), pp.5640-5646.

[152] Jiang, Z., Jiang, Z.J., Maiyalagan, T. and Manthiram, A., 2016. Cobalt oxide-coated N-and B-doped graphene hollow spheres as bifunctional electrocatalysts for oxygen reduction and oxygen evolution reactions. Journal of Materials Chemistry A, 4(16), pp.5877-5889.

[153] Wang, L., Yin, F. and Yao, C., 2014. N-doped graphene as a bifunctional electrocatalyst for oxygen reduction and oxygen evolution reactions in an alkaline electrolyte. International Journal of Hydrogen Energy, 39(28), pp.15913-15919.

[154] Kannan, R., Kim, A.R., Kim, J.S. and Yoo, D.J., 2016. 3D graphene-mixed metal oxide-supported carbon palladium quantum dot nanoarchitectures–A facile bifunctional electrocatalyst for direct ethylene glycol fuel cells and oxygen evolution reactions. International Journal of Hydrogen Energy, 41(40), pp.18033-18043.

[155] Xia, W.Y., Li, N., Li, Q.Y., Ye, K.H. and Xu, C.W., 2016. Au-$NiCo_2O_4$ supported on three-dimensional hierarchical porous graphene-like material for highly effective oxygen evolution reaction. Scientific reports, 6, p.23398.

[156] Bian, W., Yang, Z., Strasser, P. and Yang, R., 2014. A $CoFe_2O_4$/graphene nanohybrid as an efficient bi-functional electrocatalyst for oxygen reduction and oxygen evolution. Journal of Power Sources, 250, pp.196-203.

[157] Bikkarolla, S.K. and Papakonstantinou, P., 2015. $CuCo_2O_4$ nanoparticles on nitrogenated graphene as highly efficient oxygen evolution catalyst. Journal of Power Sources, 281, pp.243-251.

[158] Yu, X., Zhang, M., Yuan, W. and Shi, G., 2015. A high-performance three-dimensional Ni–Fe layered double hydroxide/graphene electrode for water oxidation. Journal of Materials Chemistry A, 3(13), pp.6921-6928.

[159] Wang, J., Zhao, R., Liu, Z. and Liu, Z., 2013. Widely tunable carrier mobility of boron nitride-embedded graphene. Small, 9(8), pp.1373-1378.

[160] Wang, H., Zhou, Y., Wu, D., Liao, L., Zhao, S., Peng, H. and Liu, Z., 2013. Synthesis of boron-doped graphene monolayers using the sole solid feedstock by chemical vapor deposition. Small, 9(8), pp.1316-1320.

[161] Singh, S.K., Kumar, D., Dhavale, V.M., Pal, S. and Kurungot, S., 2016. Strategic Preparation of Efficient and Durable NiCo Alloy Supported N-Doped Porous Graphene as an Oxygen Evolution Electrocatalyst: A Theoretical and Experimental Investigation. Advanced Materials Interfaces, 3(20).

[162] Wang, J., Lin, W.F., Shi, Y., Wang, H.S., Rong, L.Q. and Xia, X.H., 2016. A simple way to fine tune the redox potentials of cobalt ions encapsulated in nitrogen doped graphene molecular catalysts for the oxygen evolution reaction. Chemical Communications, 52(91), pp.13409-13412.

[163] Li, M., Zhang, L., Xu, Q., Niu, J. and Xia, Z., 2014. N-doped graphene as catalysts for oxygen reduction and oxygen evolution reactions: Theoretical considerations. Journal of Catalysis, 314, pp.66-72.

[164] Chen, S., Duan, J., Jaroniec, M. and Qiao, S.Z., 2013. Three-dimensional N-doped graphene hydrogel/NiCo double hydroxide electrocatalysts for highly efficient oxygen evolution. Angewandte Chemie International Edition, 52(51), pp.13567-13570.

[165] Lin, Z., Waller, G.H., Liu, Y., Liu, M. and Wong, C.P., 2013. Simple preparation of nanoporous few-layer nitrogen-doped graphene for use as an efficient electrocatalyst for oxygen reduction and oxygen evolution reactions. Carbon, 53, pp.130-136.

[166] Chen, S., Duan, J., Ran, J., Jaroniec, M. and Qiao, S.Z., 2013. N-doped graphene film-confined nickel nanoparticles as a highly efficient three-dimensional oxygen evolution electrocatalyst. Energy & Environmental Science, 6(12), pp.3693-3699.

[167] El-Sawy, A.M., Mosa, I.M., Su, D., Guild, C.J., Khalid, S., Joesten, R., Rusling, J.F. and Suib, S.L., 2016. Controlling the Active Sites of Sulfur-Doped Carbon Nanotube–Graphene Nanolobes for Highly Efficient Oxygen Evolution and Reduction Catalysis. Advanced Energy Materials, 6(5).

[168] Eftekhari, A. and Yazdani, B., 2010. Initiating electropolymerization on graphene sheets in graphite oxide structure. Journal of Polymer Science Part A: Polymer Chemistry, 48(10), pp.2204-2213.

[169] Han, X., Yu, C., Yang, J., Zhao, C., Huang, H., Liu, Z., Ajayan, P.M. and Qiu, J., 2016. Mass and Charge Transfer Coenhanced Oxygen Evolution Behaviors in CoFe-Layered Double Hydroxide Assembled on Graphene. Advanced Materials Interfaces, 3(7).

[170] Nakayama, M., Fujii, Y., Fujimoto, K., Yoshimoto, M., Kaide, A., Saeki, T. and Asada, H., 2016. Electrochemical synthesis of a nanohybrid film consisting of stacked graphene sheets and manganese oxide as oxygen evolution reaction catalyst. RSC Advances, 6(28), pp.23377-23382.

[171] Irshad, A. and Munichandraiah, N., 2016. Electrochemical deposition of manganese oxide–phosphate–reduced graphene oxide composite and electrocatalysis of the oxygen evolution reaction. RSC Advances, 6(36), pp.30552-30563.

[172] Ping, J., Wang, Y., Lu, Q., Chen, B., Chen, J., Huang, Y., Ma, Q., Tan, C., Yang, J., Cao, X. and Wang, Z., 2016. Self-Assembly of Single-Layer CoAl-Layered Double Hydroxide Nanosheets on 3D Graphene Network Used as Highly Efficient Electrocatalyst for Oxygen Evolution Reaction. Advanced Materials, 28(35), pp.7640-7645.

[173] He, B., Chen, X., Lu, J., Yao, S., Wei, J., Zhao, Q., Jing, D., Huang, X. and Wang, T., 2016. One-pot Synthesized $Co/Co_3O_4$-N-Graphene Composite as Electrocatalyst for Oxygen Reduction Reaction and Oxygen Evolution Reaction. Electroanalysis, 28, pp.2435-2443.

[174] Yuan, W., Zhao, M., Yuan, J. and Li, C.M., 2016. Ni foam supported three-dimensional vertically aligned and networked layered CoO nanosheet/graphene hybrid array as a high-performance oxygen evolution electrode. Journal of Power Sources, 319, pp.159-167.

[175] Tang, C., Wang, H.S., Wang, H.F., Zhang, Q., Tian, G.L., Nie, J.Q. and Wei, F., 2015. Spatially Confined Hybridization of Nanometer-Sized NiFe Hydroxides into Nitrogen-Doped Graphene Frameworks Leading to Superior Oxygen Evolution Reactivity. Advanced Materials, 27(30), pp.4516-4522.

[176] Zhao, H., Chen, C., Chen, D., Saccoccio, M., Wang, J., Gao, Y., Wan, T.H. and Ciucci, F., 2015. Ba 0.95 La 0.05 FeO 3− δ–multi-layer graphene as a low-cost and synergistic catalyst for oxygen evolution reaction. Carbon, 90, pp.122-129.

[177] Yan, W., Yang, Z., Bian, W. and Yang, R., 2015. $FeCo_2O_4$/hollow graphene spheres hybrid with enhanced electrocatalytic activities for oxygen reduction and oxygen evolution reaction. Carbon, 92, pp.74-83.

[178] Jeong, Y.S., Park, J.B., Jung, H.G., Kim, J., Luo, X., Lu, J., Curtiss, L., Amine, K., Sun, Y.K., Scrosati, B. and Lee, Y.J., 2015. Study on the catalytic activity of Noble metal nanoparticles on reduced graphene oxide for oxygen evolution reactions in lithium–air batteries. Nano letters, 15(7), pp.4261-4268.

[179] Zhao, Y., Sun, B., Huang, X., Liu, H., Su, D., Sun, K. and Wang, G., 2015. Porous graphene wrapped CoO nanoparticles for highly efficient oxygen evolution. Journal of Materials Chemistry A, 3(10), pp.5402-5408.

[180] Ren, X., Wang, B., Zhu, J., Liu, J., Zhang, W. and Wen, Z., 2015. The doping effect on the catalytic activity of graphene for oxygen evolution reaction in a lithium–air battery: a first-principles study. Physical Chemistry Chemical Physics, 17(22), pp.14605-14612.

[181] Cheng, M.J., Head-Gordon, M. and Bell, A.T., 2014. How to chemically tailor metal-porphyrin-like active sites on carbon nanotubes and graphene for minimal overpotential in the electrochemical oxygen evolution and oxygen reduction reactions. The Journal of Physical Chemistry C, 118(51), pp.29482-29491.

[182] Long, X., Li, J., Xiao, S., Yan, K., Wang, Z., Chen, H. and Yang, S., 2014. A strongly coupled graphene and FeNi double hydroxide hybrid as an excellent electrocatalyst for the oxygen evolution reaction. Angewandte Chemie, 126(29), pp.7714-7718.

[183] Pu, Z., Liu, Q., Asiri, A.M. and Sun, X., 2014. Ni nanoparticles-graphene hybrid film: one-step electrodeposition preparation and application as highly efficient oxygen evolution reaction electrocatalyst. Journal of Applied Electrochemistry, 44(11), pp.1165-1170.

[184] Chen, S., Duan, J., Han, W. and Qiao, S.Z., 2014. A graphene–$MnO_2$ framework as a new generation of three-dimensional oxygen evolution promoter. Chemical communications, 50(2), pp.207-209.

[185] Tian, J., Liu, Q., Asiri, A.M., Alamry, K.A. and Sun, X., 2014. Ultrathin graphitic C3N4 nanosheets/graphene composites: efficient organic electrocatalyst for oxygen evolution reaction. ChemSusChem, 7(8), pp.2125-2130.

[186] Kong, F.D., Zhang, S., Yin, G.P., Liu, J. and Xu, Z.Q., 2013. $IrO_2$-graphene hybrid as an active oxygen evolution catalyst for water electrolysis. International Journal of Hydrogen Energy, 38(22), pp.9217-9222.

[187] Liang, Y., Li, Y., Wang, H., Zhou, J., Wang, J., Regier, T. and Dai, H., 2011. $Co_3O_4$ nanocrystals on graphene as a synergistic catalyst for oxygen reduction reaction. arXiv preprint arXiv:1108.2331.

[188] Pei, S. and Cheng, H.M., 2012. The reduction of graphene oxide. Carbon, 50(9), pp.3210-3228.

[189] Stankovich, S., Dikin, D.A., Piner, R.D., Kohlhaas, K.A., Kleinhammes, A., Jia, Y., Wu, Y., Nguyen, S.T. and Ruoff, R.S., 2007. Synthesis of graphene-based nanosheets via chemical reduction of exfoliated graphite oxide. carbon, 45(7), pp.1558-1565.

[190] Robertson, J. and O'reilly, E.P., 1987. Electronic and atomic structure of amorphous carbon. Physical Review B, 35(6), p.2946.

[191] Guex, L.G., Sacchi, B., Peuvot, K., Andersson, R.L., Pourrahimi, A.M., Strom, V., Farris, S. and Olsson, R.T., 2017. Experimental review: Chemical reduction of graphene oxide (GO) to reduced graphene oxide (rGO) by aqueous chemistry. Nanoscale.

[192] Chanda, D., Hnát, J., Dobrota, A.S., Pašti, I.A., Paidar, M. and Bouzek, K., 2015. The effect of surface modification by reduced graphene oxide on the electrocatalytic activity of nickel towards the hydrogen evolution reaction. Physical Chemistry Chemical Physics, 17(40), pp.26864-26874.

[193] Zhan, Y., Xu, C., Lu, M., Liu, Z. and Lee, J.Y., 2014. Mn and Co co-substituted Fe $_3O_4$ nanoparticles on nitrogen-doped reduced graphene oxide for oxygen electrocatalysis in alkaline solution. Journal of Materials Chemistry A, 2(38), pp.16217-16223.

[194] Kater Hake, PHYSIOLOGY TODAY, National Cotton Council of America, November 1991, Volume 3, Number 2.

[195] Biodegradable Polyesters (BIOBASED) Aliphatic Polyesters, Polymer Properties Database, http://polymerdatabase.com/polymer%20classes/Biodegradable%20Polyester%20type.html, Last visited on 12/13/2017.

[196] Robert B. Waddell, Bioscouring of cotton: Commercial applications of alkaline stable pectinase, AATCC Review, 2(4), 2002.

[197] Moore's law for fibers, http://go.affoa.org/moores-law, Last visited on 12/13/17.

[198] Zhao, C., Shao, X., Zhang, Y. and Qian, X., 2016. $Fe_2O_3$/Reduced Graphene Oxide/$Fe_3O_4$ Composite in Situ Grown on Fe Foil for High-Performance Supercapacitors. ACS applied materials & interfaces, 8(44), pp.30133-30142.

[199] Stern, L.A. and Hu, X., 2015. Enhanced oxygen evolution activity by $NiO_x$ and Ni $(OH)_2$ nanoparticles. Faraday discussions, 176, pp.363-379.

[200] Yang Qiu, Le Xin, and Wenzhen Li, Electrocatalytic Oxygen Evolution over Supported Small Amorphous Ni–Fe Nanoparticles in Alkaline Electrolyte, Langmuir, 2014, 30 (26), pp 7893–7901.

[201] Kuai, L., Geng, J., Chen, C., Kan, E., Liu, Y., Wang, Q. and Geng, B., 2014. A Reliable Aerosol-Spray-Assisted Approach to Produce and Optimize Amorphous Metal Oxide Catalysts for Electrochemical Water Splitting. Angewandte Chemie, 126(29), pp.7677-7681.

[202] Minrui Gao, Wenchao Sheng, Zhongbin Zhuang, Qianrong Fang, Shuang Gu, Jun Jiang, and Yushan Yan, Efficient Water Oxidation Using Nanostructured α-Nickel-Hydroxide as an Electrocatalyst, J. Am. Chem. Soc., 2014, 136 (19), pp 7077–7084.

[203] Shannon Klaus, Yun Cai, Mary W. Louie, Lena Trotochaud, and Alexis T. Bell, Effects of Fe Electrolyte Impurities on $Ni(OH)_2$/NiOOH Structure and Oxygen Evolution Activity, J. Phys. Chem. C, 2015, 119 (13), pp 7243–7254.

[204] Zhou, W., Wu, X.J., Cao, X., Huang, X., Tan, C., Tian, J., Liu, H., Wang, J. and Zhang, H., 2013. $Ni_3S_2$ nanorods/Ni foam composite electrode with low overpotential for electrocatalytic oxygen evolution. Energy & Environmental Science, 6(10), pp.2921-2924.

[205] Feng, L.L., Yu, G., Wu, Y., Li, G.D., Li, H., Sun, Y., Asefa, T., Chen, W. and Zou, X., 2015. High-index faceted $Ni_3S_2$ nanosheet arrays as highly active and ultrastable electrocatalysts for water splitting. J. Am. Chem. Soc, 137(44), pp.14023-14026.

[206] Zhu, W., Yue, X., Zhang, W., Yu, S., Zhang, Y., Wang, J. and Wang, J., 2016. Nickel sulfide microsphere film on Ni foam as an efficient bifunctional electrocatalyst for overall water splitting. Chemical Communications, 52(7), pp.1486-1489.

[207] Tang, C., Cheng, N., Pu, Z., Xing, W. and Sun, X., 2015. NiSe nanowire film supported on nickel foam: an efficient and stable 3D bifunctional electrode for full water splitting. Angewandte Chemie, 127(32), pp.9483-9487.

[208] Shi, J., Hu, J., Luo, Y., Sun, X. and Asiri, A.M., 2015. $Ni_3Se_2$ film as a non-precious metal bifunctional electrocatalyst for efficient water splitting. Catalysis Science & Technology, 5(11), pp.4954-4958.

[209] Liu, T., Asiri, A.M. and Sun, X., 2016. Electrodeposited Co-doped $NiSe_2$ nanoparticles film: a good electrocatalyst for efficient water splitting. Nanoscale, 8(7), pp.3911-3915.

[210] Kwak, I.H., Im, H.S., Jang, D.M., Kim, Y.W., Park, K., Lim, Y.R., Cha, E.H. and Park, J., 2016. $CoSe_2$ and $NiSe_2$ nanocrystals as superior bifunctional catalysts for electrochemical and photoelectrochemical water splitting. ACS applied materials & interfaces, 8(8), pp.5327-5334.

[211] Xu, X., Song, F. and Hu, X., 2016. A nickel iron diselenide-derived efficient oxygen-evolution catalyst. Nature communications, 7.

[212] Pu, Z., Luo, Y., Asiri, A.M. and Sun, X., 2016. Efficient electrochemical water splitting catalyzed by electrodeposited nickel diselenide nanoparticles based film. ACS applied materials & interfaces, 8(7), pp.4718-4723.

[213] Gorlin, Y. and Jaramillo, T.F., 2010. A bifunctional nonprecious metal catalyst for oxygen reduction and water oxidation. Journal of the American Chemical Society, 132(39), pp.13612-13614.

[214] Wang, Z., Li, J., Tian, X., Wang, X., Yu, Y., Owusu, K.A., He, L. and Mai, L., 2016. Porous Nickel–Iron Selenide Nanosheets as Highly Efficient Electrocatalysts for Oxygen Evolution Reaction. ACS applied materials & interfaces, 8(30), pp.19386-19392.

[215] Umanga De Silva, Jahangir Masud, Ning Zhang, Yu Hong, Wipula P. R. Liyanage, Mohsen Asle Zaeem, Manashi Nath, Nickel telluride as a bifunctional electrocatalyst for efficient water splitting in alkaline medium, Submitted to Energy and Environmental Science.

[216] Masa, J., Sinev, I., Mistry, H., Ventosa, E., de la Mata, M., Arbiol, J., Muhler, M., Roldan Cuenya, B. and Schuhmann, W., 2017. Ultrathin High Surface Area Nickel Boride ($Ni_xB$) Nanosheets as Highly Efficient Electrocatalyst for Oxygen Evolution. Advanced Energy Materials.

[217] Jiang, J., Wang, M., Yan, W., Liu, X., Liu, J., Yang, J. and Sun, L., 2017. Highly active and durable electrocatalytic water oxidation by a $NiB_{0.45}/NiO_x$ core-shell heterostructured nanoparticulate film. Nano Energy.

[218] Umapathi, S., Masud, J., Swesi, A.T. and Nath, M., 2017. $FeNi_2Se_4$–Reduced Graphene Oxide Nanocomposite: Enhancing Bifunctional Electrocatalytic Activity for Oxygen Evolution and Reduction through Synergistic Effects. Advanced Sustainable Systems, 1(10).

# VITA

Maalavan Arivu was born in Chennai, Tamil Nadu, India. He attained his Bachelor of Technology degree in Aerospace Engineering in May 2015 with focus on ‘materials and structures’ from Amrita Vishwa Vidyapeetham, Coimbatore, Tamil Nadu, India. He then went on to pursue Master of Science degree in Materials Science and Engineering as a graduate student at Missouri University of Science and Technology, and performed his thesis under the guidance of Dr. Manashi Nath and received his degree in May 2018. His areas of interest are nanomaterials synthesis, carbon based materials and electrochemical capacitance.